


Lattice Boltzmann model for weakly compressible flows

Praveen Kumar Kolluru , Mohammad Atif , Manjusha Namburi , and Santosh Ansumali *
Jawaharlal Nehru Centre for Advanced Scientific Research, Jakkur, Bangalore 560064, India

 (Received 15 September 2019; published 22 January 2020)

We present an energy conserving lattice Boltzmann model based on a crystallographic lattice for simulation of weakly compressible flows. The theoretical requirements and the methodology to construct such a model are discussed. We demonstrate that the model recovers the isentropic sound speed in addition to the effects of viscous heating and heat flux dynamics. Several test cases for acoustics and thermal and thermoacoustic flows are simulated to show the accuracy of the proposed model.

DOI: [10.1103/PhysRevE.101.013309](https://doi.org/10.1103/PhysRevE.101.013309)

I. INTRODUCTION

The lattice Boltzmann (LB) method with its simplified kinetic description of hydrodynamics in terms of a sequence of collision and free flight restricted on a D -dimensional lattice provides a computationally efficient and easily parallelizable alternative simulation methodology [1–3]. An LB model in its standard formulation describes a weakly compressible flow at a reference temperature T_0 . The pressure p and the mass density ρ are related via the ideal equation of state $p = \rho\theta_0$, where $\theta_0 = k_B T_0/m$ is the scaled temperature with k_B as the Boltzmann constant and m is the mass of the molecule. These models are quite suitable for isothermal flows where the relevant timescale is a few orders of magnitude higher than the acoustic timescales and the object of interest is the velocity or vorticity field. A consequence of kinetic equation with an isothermal dynamics, as revealed by Chapman-Enskog expansion, is that in the hydrodynamic limit, the stress tensor is not traceless and is of form [1,4]

$$\sigma_{\alpha\beta} = \eta(\partial_\alpha u_\beta + \partial_\beta u_\alpha), \quad (1)$$

which implies that the bulk viscosity $\zeta = 2/3\eta$, where η is the shear viscosity. Even though this expression for bulk viscosity is not realistic for any fluid, this is not of too much concern as long as one is interested in the velocity dynamics in the limit of vanishing Mach number Ma . This is due to the fact that the divergence of the velocity field for low Mach number is $\partial_\kappa u_\kappa \sim O(Ma^2)$ [5]. Thus, the method is routinely used for incompressible hydrodynamic simulations both in low Reynolds number creeping flow regime as well as for high Reynolds number turbulent flow regime [1–3,6–9].

An extension of the lattice Boltzmann method (LBM) for acoustics is relatively recent [5,10–15]. These works have established the capability of LBM to correctly reproduce fundamental acoustic phenomena and highlighted the low dissipative behavior of the LBM. The starting point for acoustic modeling in isothermal LB is the fact that the pressure fluctuation δp (linearized around no flow condition) for the

method follows the wave equation [16]

$$\frac{\partial^2 \delta p}{\partial t^2} = \bar{c}_s^2 \nabla^2 \delta p, \quad (2)$$

with the isothermal sound speed being $\bar{c}_s \equiv \sqrt{\partial p / \partial \rho|_T} = \sqrt{\theta_0}$. We remind that the sound wave is generated by compression and expansion of air and is not an isothermal but an adiabatic process. Thus, it is not surprising that neglecting the rapidly fluctuating temperature field in a sound wave leads to an incorrect value of the sound speed. The real isentropic sound speed is $c_s = \sqrt{\partial p / \partial \rho|_s} = \sqrt{\gamma\theta}$, where γ is the specific heat ratio. However, in practice for simulating acoustic waves, this incorrect sound speed is not of too much concern, as dynamics can be corrected via rescaling of temperature. In particular, Eq. (2) describes the correct acoustic dynamics at temperature $\theta = \theta_0/\gamma$.

However, a more elaborate description of the sound wave in LB framework must start from the true evolution equation for pressure fluctuation obtained by Navier-Stokes-Fourier (NSF) equation linearized around no flow condition as [17]

$$\left[-\frac{\partial^2}{\partial t^2} + \frac{\Gamma}{\rho_0} \frac{\partial}{\partial t} \nabla^2 \right] \delta \rho + \nabla^2 \delta p = 0, \quad (3)$$

where $\delta \rho$ is the density fluctuation from the equilibrium density ρ_0 and $\Gamma = 4\eta/3 + \zeta$. The thermodynamic equation of state relates the density and pressure fluctuations with the entropy fluctuation via the relation [18]

$$\delta \rho = \frac{\partial \rho}{\partial p} \Big|_s \delta p + \frac{\partial \rho}{\partial s} \Big|_p \delta s, \quad (4)$$

where the entropy density fluctuation δs satisfies the relation [16]

$$\frac{\partial \delta s}{\partial t} = -\frac{1}{\rho_0 T_0} \nabla_\alpha \delta q_\alpha, \quad (5)$$

with the heat flux due to the temperature fluctuation δq_α obeying the Fourier's law, i.e., $\delta q_\alpha = -\kappa \nabla_\alpha \delta T$ where κ is the thermal conductivity [19].

*ansumali@jncasr.ac.in

Thus, the final evolution equation for the pressure fluctuation obtained using Eqs. (3) and (4) is

$$\left[-\frac{\partial^2}{\partial t^2} + \frac{1}{\rho_0} \Gamma \frac{\partial}{\partial t} \nabla^2 \right] \left(\frac{\partial \rho}{\partial p} \Big|_s \delta p + \frac{\partial \rho}{\partial s} \Big|_p \delta s \right) + \nabla^2 \delta p = 0, \quad (6)$$

where the entropy fluctuation is governed by Eq. (5). For short time dynamics, i.e., at timescales much less than the momentum diffusion timescales, the dynamics can be considered to be isentropic and entropy fluctuations as well as the viscous contribution can be ignored. This reduces Eq. (6) to the wave equation as solved by an isothermal LB model given in Eq. (2). However, a faithful simulation of acoustics by LB models requires that for a linearized flow, the pressure fluctuations obey Eq. (6), which in turn demands accurate heat flux dynamics via Eq. (5). Hence, a model suitable for acoustic simulations should have the following features:

- (i) the right form of bulk viscosity and isentropic sound speed;
- (ii) correct heat flux dynamics to accurately capture the dynamics of pressure fluctuations;
- (iii) the correct specific heat ratio and the Prandtl number.

Many of these defects disappear if one works with an energy conserving LB model [4]. For example, it was shown in Ref. [4] that the unphysical bulk viscosity does not exist in energy conserving models. It was further noted in subsequent works that the energy conserving LB models recover the isentropic sound speed [20]. Energy conserving models on lower order lattices such as *D3Q27* are restricted to very small temperature fluctuations as the heat flux shows a significant departure from Fourier's law. Early work was done in Refs. [21,22] to incorporate temperature dynamics in LB using energy conserving equilibrium [23], and the notion of guided equilibrium to cancel the error terms in the moments of discrete equilibrium [24,25]. In this work, we use multispeed lattices without changing the collision. It is known that multispeed models recover the heat flux dynamics to a higher order of accuracy [26,27]. For example, recently a higher-order body centered cubic (bcc) lattice model was proposed for thermal dynamics [27]. In this work, we propose another higher-order lattice Boltzmann model for acoustic simulations and restrict ourselves to the specific heat ratio of a monoatomic ideal gas and the Prandtl number to unity.

In particular, we propose an energy conserving multispeed LBM with 41 discrete velocities in three dimensions that is relevant for acoustics and weakly compressible flows. We list the conditions on the equilibrium for the discrete velocity models to recover the Navier-Stokes-Fourier equations as the hydrodynamic limit. We also discuss the importance of the cubic accuracy in recovering the Navier-Stokes hydrodynamics. We develop the LB model based on recently proposed crystallographic lattice Boltzmann framework using a bcc lattice [6]. It was shown that the bcc lattice gives better spatial accuracy in addition to more accuracy in the velocity space, in comparison to a simple cubic (sc) lattice. We outline the procedure for the development of the discrete equilibrium using entropic formulation by a series expansion at the reference state with zero velocity and zero temperature variation. First, the equilibrium at a rest state is derived for nonzero

variation in temperature, and a nonzero velocity equilibrium is derived as a series expansion around the earlier reference state. This expansion is more stable than a direct two variable (Mach number and deviation from reference temperature) expansion. Finally, we show the capability of the proposed model to perform aeroacoustic, thermal, thermoacoustic, and turbulent simulations by presenting a number of benchmark simulations.

The paper is structured as follows: In Sec. II we describe the lattice Boltzmann method briefly and define the restrictions on the discrete velocity model to recover isothermal compressible hydrodynamics. This is followed by a derivation of a compressible thermohydrodynamic model and constraints for such a model in Sec. III. A brief description on recently proposed class of crystallographic lattice Boltzmann models and followed by the construction of a different LB model, *RD3Q41* model, with 41 velocities on a bcc lattice is given in Sec. IV. An energy conserving equilibrium distribution function is derived for the proposed *RD3Q41* model in Sec. V. We show the capability of this model for simulating acoustic phenomena in Sec. VI, followed by a few test cases to demonstrate its ability to simulate thermal flows in Sec. VII. A nontrivial problem involving both thermal and acoustic phenomena is presented in Sec. VIII. Further, in Sec. IX we show that the proposed model is also advantageous for multiphase flows on account of it being more accurate in the velocity space. Finally, we simulate a few turbulent flows at high Reynolds numbers like the Kida-Peltz flow, flow in a rectangular channel, and flow past a sphere in Sec. X.

II. LATTICE BOLTZMANN METHOD

The lattice Boltzmann method (LBM) with its simplified kinetic picture on a D -dimensional lattice provides a computationally efficient description of hydrodynamics [1,2]. In this section, we briefly review the method and the basic motivation behind its use for simulating hydrodynamics. In LBM, the velocity space is discretized to a finite set $\mathcal{C} = \{\mathbf{c}_i, i = 1 \dots N_d\}$ and one associates a discrete population $f_i \in \mathbf{f}$ with each \mathbf{c}_i . The discrete populations $f(\mathbf{c}_i, \mathbf{x}, t) \equiv f_i(\mathbf{x}, t)$ are considered a function of location \mathbf{x} and time t . The set \mathcal{C} is chosen to satisfy an appropriate set of symmetries needed to recover hydrodynamics from the evolution equation of f_i in the long time limit [28]. The hydrodynamic variables such as the mass density ρ , velocity \mathbf{u} , and the energy E are defined as

$$\rho = \langle f, 1 \rangle, \quad \mathbf{j} \equiv \rho \mathbf{u} = \langle f, \mathbf{c} \rangle, \quad E = \left\langle f, \frac{\mathbf{c}^2}{2} \right\rangle, \quad (7)$$

where the inner product between two functions of discrete velocities ϕ and ψ is defined as

$$\langle \phi, \psi \rangle = \sum_{i=1}^{N_d} \phi_i \psi_i. \quad (8)$$

In a three-dimensional space ($D = 3$), the energy is that of the ideal gas, i.e., $E = (\rho u^2 + 3\rho\theta)/2$.

A few higher-order moments which are relevant to the hydrodynamic description are momentum flux as $P_{\alpha\beta} = \langle f, \mathbf{c}_\alpha \mathbf{c}_\beta \rangle$, flux of momentum flux as $Q_{\alpha\beta\gamma} = \langle f, \mathbf{c}_\alpha \mathbf{c}_\beta \mathbf{c}_\gamma \rangle$. The fluctuating velocity ξ is defined as $\mathbf{c} - \mathbf{u}$ and the heat

flux as $q_\alpha = \langle f, \xi_\alpha \xi^2 / 2 \rangle$ and the flux of heat flux as $R_{\alpha\beta} = \langle f, \xi^2 \xi_\alpha \xi_\beta \rangle$.

Typically, one works with the discrete in space and time version of the kinetic evolution equation in the Boltzmann Bhatnagar-Gross-Krook (BGK) form [29] as

$$f_i(\mathbf{x} + \mathbf{c}_i \Delta t, t + \Delta t) = f_i(\mathbf{x}, t) + 2\beta [f_i^{\text{eq}}(\rho(\mathbf{f}), \mathbf{u}(\mathbf{f})) - f_i(\mathbf{x}, t)], \quad (9)$$

where f_i^{eq} represent discrete form of the Maxwell-Boltzmann equilibrium, Δt is the chosen time step, and $\beta = \Delta t / (2\tau + \Delta t)$ with τ as the mean free time. The dimensionless parameter β , bounded in the interval $0 < \beta < 1$ with $\beta = 1$ as the dissipationless state, physically represents the discrete dimensionless relaxation toward the equilibrium. Here, the choice of the discrete version of equilibrium distribution f_i^{eq} is crucial for recovering the correct hydrodynamic limit and different formulations of lattice Boltzmann models differ mainly in the choice of this discrete equilibrium [23,30]. A common choice is to project the Maxwell-Boltzmann distribution on the Hermite basis to get a computationally attractive polynomial expression of the equilibrium as [31–34]

$$f_i^{\text{eq}}(\rho, \mathbf{u}) = w_i \rho \left[1 + \frac{u_\alpha c_{i\alpha}}{\theta_0} + \frac{u_\alpha u_\beta}{2\theta_0^2} (c_{i\alpha} c_{i\beta} - \theta_0 \delta_{\alpha\beta}) \right], \quad (10)$$

where θ_0 is some reference temperature associated with the underlying lattice and w_i are the weights chosen in such a way that the mass and momentum constraints are ensured, i.e.,

$$\sum_{i=1}^{N_d} f_i^{\text{eq}} = \rho, \quad \sum_{i=1}^{N_d} f_i^{\text{eq}} c_{i\alpha} = j_\alpha. \quad (11)$$

Furthermore, to get correct hydrodynamic limit for isothermal low Mach number dynamics, it is essential to ensure that the second moment of the discrete equilibrium is the same as that obtained from the Maxwell-Boltzmann distribution, i.e.,

$$P_{\alpha\beta}^{\text{eq}} = \sum_{i=1}^{N_d} f_i^{\text{eq}} c_{i\alpha} c_{i\beta} = \rho u_\alpha u_\beta + \rho \theta_0 \delta_{\alpha\beta}. \quad (12)$$

The rationale for adding Eq. (12) can be understood by writing first the kinetic equation in its partial differential form (PDE) form (for $\Delta t \rightarrow 0$) [26,28,35] as

$$\partial_t f_i + c_{i\alpha} \partial_\alpha f_i = -\frac{1}{\tau} [f_i - f_i^{\text{eq}}], \quad (13)$$

from which one can write the mass and momentum conservation laws as

$$\begin{aligned} \partial_t \rho + \partial_\alpha j_\alpha &= 0, \\ \partial_t j_\alpha + \partial_\beta P_{\alpha\beta} &= 0. \end{aligned} \quad (14)$$

The evolution equation for the pressure tensor $P_{\alpha\beta}$ using Eqs. (12) and (13) as

$$\partial_t P_{\alpha\beta} + \partial_\gamma Q_{\alpha\beta\gamma} = \frac{1}{\tau} (\rho u_\alpha u_\beta + \rho \theta_0 \delta_{\alpha\beta} - P_{\alpha\beta}), \quad (15)$$

from which it is evident that in the limit of $\tau \rightarrow 0$, $P_{\alpha\beta} \rightarrow \rho u_\alpha u_\beta + \rho \theta_0 \delta_{\alpha\beta}$, and thus the zeroth-order hydrodynamic equation describes the inviscid hydrodynamics as given by

the Euler equation. The Navier-Stokes hydrodynamics is recovered provided [32,36,37]

$$\sum_i^{N_d} f_i^{\text{eq}} c_{i\alpha} c_{i\beta} c_{i\gamma} = \rho u_\alpha u_\beta u_\gamma + \rho \theta_0 (u_\alpha \delta_{\beta\gamma} + u_\beta \delta_{\alpha\gamma} + u_\gamma \delta_{\alpha\beta}). \quad (16)$$

In most of the widely used lower-order lattice Boltzmann models, the above condition is satisfied only up to linear order in velocity due to the absence of the cubic term in the equilibrium represented by Eq. (10) [38].

Equation (10) along with Eqs. (11) and (12) imply that the discrete velocity set and associated weights should satisfy

$$\begin{aligned} \sum_{i=1}^{N_d} w_i &= 1, \quad \sum_{i=1}^{N_d} w_i c_{i\alpha} c_{i\beta} = \theta_0 \delta_{\alpha\beta}, \\ \sum_{i=1}^{N_d} w_i c_{i\alpha} c_{i\beta} c_{i\gamma} c_{i\zeta} &= \theta_0^2 \Delta_{\alpha\beta\gamma\zeta}, \end{aligned} \quad (17)$$

where $\Delta_{\alpha\beta\gamma\zeta} = \delta_{\alpha\beta} \delta_{\gamma\zeta} + \delta_{\alpha\gamma} \delta_{\beta\zeta} + \delta_{\alpha\zeta} \delta_{\beta\gamma}$ is the fourth-order isotropic tensor and all odd-order moments, such as

$$\begin{aligned} \sum_{i=1}^{N_d} w_i c_{i\alpha} &= 0, \quad \sum_{i=1}^{N_d} w_i c_{i\alpha} c_{i\beta} c_{i\gamma} = 0, \\ \sum_{i=1}^{N_d} w_i c_{i\alpha} c_{i\beta} c_{i\gamma} c_{i\kappa} c_{i\zeta} &= 0, \end{aligned} \quad (18)$$

are zero. These conditions are central to models for isothermal incompressible hydrodynamics, and the procedure to construct them is well understood [1]. It should be noted here that in case of compressible hydrodynamics, moment chain suggests that one needs to add $O(u^3)$ contribution in the equilibrium distribution so that Eq. (16) is satisfied. This condition on the third moment can be fulfilled only if the discrete equilibrium distribution is of the form [35]

$$\begin{aligned} f_i^{\text{eq}} &= w_i \left(1 + \frac{u_\alpha c_{i\alpha}}{\theta_0} + \frac{u_\alpha u_\beta}{2\theta_0^2} (c_{i\alpha} c_{i\beta} - \theta_0 \delta_{\alpha\beta}) \right. \\ &\quad \left. + \frac{u_\alpha u_\beta u_\gamma c_{i\gamma}}{6\theta_0^3} (c_{i\alpha} c_{i\beta} - 3\theta_0 \delta_{\alpha\beta}) \right). \end{aligned} \quad (19)$$

This adds further restriction on the weights as

$$\sum_{i=1}^{N_d} w_i c_{i\alpha} c_{i\beta} c_{i\gamma} c_{i\kappa} c_{i\zeta} c_{i\eta} = \theta_0^3 \Delta_{\alpha\beta\gamma\kappa\zeta\eta}, \quad (20)$$

where $\Delta_{\alpha\beta\gamma\kappa\zeta\eta}$ is the sixth-order isotropic tensor [28]. However, only very high-order on-lattice models are known to satisfy such constraint in three dimensions [35,39]. In practice, it is easier to satisfy the contracted version of Eq. (16),

$$\sum_{i=1}^{N_d} f_i^{\text{eq}} c_i^2 c_{i\alpha} = \rho u_\alpha u^2 + (D+2) \rho \theta_0 u_\alpha, \quad (21)$$

which implies

$$\sum_{i=1}^{N_d} w_i c_i^2 c_{i\alpha} c_{i\beta} c_{i\gamma} c_{i\kappa} = 7\theta_0^3 \Delta_{\alpha\beta\gamma\kappa}. \quad (22)$$

The above condition only ensures that the evolution equation for the energy is correct to the leading order. The implications of the recovered energy equation are that the bulk viscosity and the sound speed are recovered accurately. The models that lack the conditions given in Eqs. (21) and (22) have the thermal conductivity dependent on the local velocity and local temperature even at the lowest order. In this work, we will consider Eqs. (21) and (22) as a requirement on higher-order LBM.

III. COMPRESSIBLE THERMOHYDRODYNAMICS

In the previous section, the requirements for constructing a model for isothermal compressible hydrodynamics and the importance of the cubic accuracy in recovering the Navier-Stokes hydrodynamics has been described. It is known that on higher-order lattices such cubic accuracy can be imposed [28,40]. However, typically, this has been done in an isothermal setting. A drawback of such models, though, is that the isentropic speed of sound is not recovered and they also lack the coupling between thermal and acoustic modes [20]. These aspects have not gotten enough attention in the development of new LB models.

The coupling between thermal and acoustic modes requires an accurate description of heat flux [41,42]. In particular, in the limit of low Knudsen number, one must recover Fourier dynamics. Hence, Navier-Stokes-Fourier dynamics should be recovered as the first-order hydrodynamic description in the compressible models with energy conservation.

The heat flux is given by Fourier law via Chapman-Enskog analysis requires that the evolution for the energy flux

$$\partial_t q_\alpha + \partial_\beta R_{\alpha\beta} = \frac{1}{\tau} (q_\alpha^{\text{eq}} - q_\alpha) \quad (23)$$

is correct at the leading order

$$\partial_t^{(0)} q_\alpha^{\text{eq}} + \partial_\beta R_{\alpha\beta}^{\text{eq}} = \frac{1}{\tau} (-q_\alpha^{\text{neq}}). \quad (24)$$

Since only the trace of the equilibrium of the fourth-order moment in the Maxwell-Boltzmann form appears in the balance equation of heat flux, we only need to ensure

$$R_{\alpha\beta}^{\text{eq}}(\mathbf{u} = 0) = 5\rho\theta^2\delta_{\alpha\beta} \quad (25)$$

to get the evolution of heat flux at least to be quadratically correct in terms of $\Delta\theta = \theta/\theta_0 - 1$, the dimensionless departure of θ from θ_0 .

In order to ensure that $R_{\alpha\beta}$ satisfy Eq. (25), we write the equilibrium at $\mathbf{u} = 0$ as

$$\tilde{f}_i = w_i \rho \left[1 + \frac{\Delta\theta}{2} \left(\frac{c_i^2}{\theta_0} - 3 \right) + \frac{\Delta^2\theta}{8} \left(\frac{c_i^4}{\theta_0^2} - 10 \frac{c_i^2}{\theta_0} + 15 \right) \right]. \quad (26)$$

The expected value of $R_{\alpha\beta}^{\text{eq}}$ computed with this equilibrium matches the required value

$$R_{\alpha\beta}^{\text{eq}}(\mathbf{u} = 0) = 5\rho\theta_0^2\delta_{\alpha\beta}(1 + 2\Delta\theta + \Delta^2\theta) = 5\rho\theta^2\delta_{\alpha\beta}, \quad (27)$$

provided the model satisfies

$$\sum_{i=1}^{N_d} w_i c_i^8 = 945\theta_0^4. \quad (28)$$

This condition is not considered by some extensions of LBM where the cubic moment is imposed [35,43], where as it is considered in Ref. [27].

Thus, we look for LB models which satisfy Eqs. (17), (22), and (28). These tensorial set of equations can be simplified further for the class of discrete velocity models with the discrete velocity set \mathbf{c} which ensure isotropy and avoid preference to any direction in particular. These discrete velocity sets should have the properties of closure under inversion (if $c_i \in \mathbf{c}$ then $-c_i \in \mathbf{c}$) and closure under reflection [if $c_i(c_{ix}, c_{iy}, c_{iz}) \in \mathbf{c}$, then all possible reflections of $c_i \in \mathbf{c}$] to ensure that any vector $\psi(\mathbf{c}^2)$ in the discrete case we have

$$\begin{aligned} \langle \psi, c_x^{2n} \rangle &= \langle \psi, c_y^{2n} \rangle = \langle \psi, c_z^{2n} \rangle, \\ \langle \psi, c_x^{2n} c_y^{2m} \rangle &= \langle \psi, c_y^{2n} c_z^{2m} \rangle = \langle \psi, c_z^{2n} c_x^{2m} \rangle, \\ \langle \psi, c_x^{2n+1} \rangle &= \langle \psi, c_y^{2n+1} \rangle = \langle \psi, c_z^{2n+1} \rangle = 0, \end{aligned} \quad (29)$$

where n and m are the natural numbers [28].

The above constraints on the discrete velocity set along with Eqs. (17), (22), and (28) give us the following set of seven equations as the constraints on the weights for the proposed model as

$$\begin{aligned} \sum w_i &= 1, \quad \sum w_i c_{ix}^2 = \theta_0, \quad \sum w_i c_{ix}^4 = 3\theta_0^2, \\ \sum w_i c_{ix}^2 c_{iy}^2 &= \theta_0^2, \quad \sum w_i c_{ix}^4 c_i^2 = 21\theta_0^3, \\ \sum w_i c_{ix}^2 c_i^4 &= 35\theta_0^3, \quad \sum w_i c_i^8 = 945\theta_0^4. \end{aligned} \quad (30)$$

As reference temperature θ_0 is not specified and is an unknown, we have six more additional degrees of freedom. Hence, to obtain an on-lattice model we need six energy shells each with a weight w_i to solve the system of equations exactly. Furthermore, these weights should be positive.

IV. CRYSTALLOGRAPHIC LATTICE BOLTZMANN MODEL

Historically, the lattice chosen for the LBM has been the simple cubic (sc) lattice which demands that the grid is refined near the solid body or in zones of extreme flow variations. A recently proposed class of LBM models known as crystallographic LBM show an important connection between crystallography, optimal packing problem in the efficient discretization of PDE [6].

Based on this connection, it was argued that the optimal spatial discretization is provided by a body centered cubic (bcc) arrangement of grid points and not by a simple cubic arrangement of grid points as used by conventional structured grid based methods [6,27,44].

This lattice comprises of two simple cubic lattices displaced by a distance of $0.5\Delta x$ in each direction. Figure 1 depicts the building blocks and the links of a bcc lattice in two dimensions for illustration purpose.

Another well known fact in the computer graphics literature is that the volume representation (or rendering) is better on the bcc lattice [45]. As the bcc grid has more points at the boundaries, it was also found to represent the boundaries well. To illustrate the difference between sc and bcc lattices, we show a depiction of a sphere and an ellipsoid on both sc and bcc lattices with equal number of total lattice points in Fig. 2.

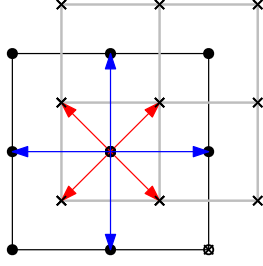


FIG. 1. Building block of a crystallographic lattice in two dimensions: simple cubic links (blue) and body centered links (red) are depicted here.

Additionally, this class of bcc lattices removes an important artifact of sc lattices with velocity component unity ($D3Q15$, $D3Q27$) of imposing an artificial closure on the third-order moments where

$$\langle f, c_\alpha^3 \rangle = c^2 \langle f, c_\alpha \rangle. \quad (31)$$

This effect plays an important role in regimes where the Knudsen boundary layer is important [46]. Like the traditional sc grids, the bcc grid also preserves the ease of streaming along the links while increasing the local accuracy.

The proposed model has 41 velocities with five different energy shells and is referred to as $RD3Q41$ model hereafter. Figure 3 shows the building blocks of the $RD3Q41$ model. The weights are derived by imposing the constraints from Eq. (30). It has one zero-velocity shell, two sc shells, one face centered cubic (fcc) shell, and two bcc energy shells. To satisfy the isotropy conditions up to machine precision, we exploit them to numerically calculate the weights. For example, $\sum_i w_i = 1$ gives

$$w_0 = 1 - 6w_{sc-1} - 6w_{sc-2} - 12w_{fcc-2} - 8w_{bcc-1} - 8w_{bcc-\frac{1}{2}}. \quad (32)$$

The energy shells and corresponding velocity sets with weights for this model are given in Table I.

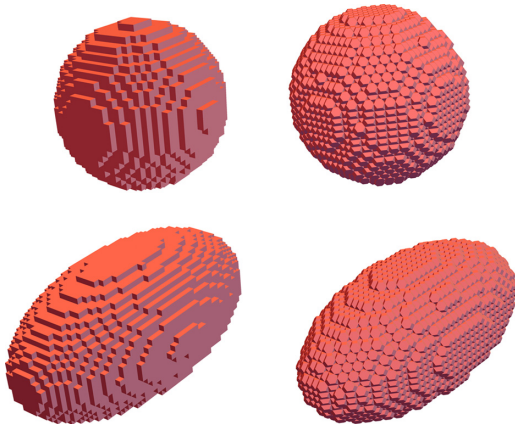


FIG. 2. A representation of a sphere and an ellipsoid with equal number of total lattice points $2N^3$ points on sc (left) and N^3 points on bcc (right) lattices.

V. DISCRETE ENTROPIC EQUILIBRIUM

The entropic formulation of the LBM restores the thermodynamic consistency embedded in the Boltzmann description. In this method, one starts with a discrete H function typically in the Boltzmann form

$$H = \sum_{i=1}^{N_d} f_i \left(\log \frac{f_i}{w_i} - 1 \right), \quad (33)$$

and construct equilibrium as its minimizer under the constraints of local conservation laws [4,23,30,47–51]. Typically, the equilibrium is constructed in an isothermal setting which lacks energy conservation. In higher-order LBM, energy conservation is included in deriving the thermal entropic equilibrium distribution.

In this section, we briefly derive the energy conserving equilibrium for the case of small temperature variation around reference temperature θ_0 using the entropic LBM. It should be reminded that in the case of entropic lattice Boltzmann model, for every discrete velocity model, one finds the Lagrange multiplier with a high degree of accuracy to preserve the positive form of equilibrium [52]. This is typically done numerically. To analyze the hydrodynamic limit of LBM, we derive the series form of the equilibrium. This allows us to calculate the closed-form expression for the moments. These expressions for the moments are relevant for analyzing the errors in the hydrodynamic limit.

Following Refs. [4,27], we consider energy conserving equilibrium and include energy in the set of constraints to obtain the equilibrium distribution which minimizes entropy [Eq. (33)] as

$$f_i^{\text{eq}} = w_i \rho \exp(-\alpha - \beta_\kappa c_{i\kappa} - \gamma c_i^2), \quad (34)$$

where α , β_κ , γ are the Lagrange multipliers associated with mass, momentum and energy, respectively [4,23]. The explicit expression can be obtained by inverting the following relations:

$$\langle f_i^{\text{eq}}, \{1, c_{i\alpha}, c^2\} \rangle = \{\rho, \rho u_\alpha, \rho u^2 + 3\rho\theta\}. \quad (35)$$

However, other than a few special cases such as the $D1Q3$ model and its higher dimension extensions $D2Q9$ and $D3Q27$, the explicit solutions are not known [4,23]. The system of equations in Eq. (35) are not explicitly invertible, therefore, we choose a reference state with mean velocity $u_\alpha = 0$ where $\beta_\kappa = 0$. Thus, the system of equations simplifies as

$$\begin{aligned} \exp(-\alpha^0) \sum_{i=1}^{N_d} w_i \exp(-\gamma^0 c_i^2) \{1, c_i^2\} \\ = \{1, 3\theta\} \equiv \{1, 3\theta_0(1 + \eta)\}, \end{aligned} \quad (36)$$

where α^0 and γ^0 are Lagrange multipliers corresponding to the state $\mathbf{u} = \mathbf{0}$. However, even for $\mathbf{u} = \mathbf{0}$, explicit solutions for other Lagrange multipliers are not known for most of the models [4]. Therefore, at $u_\alpha = 0$ itself we chose another reference state $\theta = \theta_0$ for which it is trivial to check that the solution is $\alpha^0(\theta = \theta_0) = 0$ and $\gamma^0(\theta = \theta_0) = 0$.

Following the procedure of Ref. [27], a perturbative series around this reference state can be built by expanding the Lagrange multipliers around $\alpha^{(0)}$ and $\gamma^{(0)}$ in powers of the smallness parameter $\eta = \theta/\theta_0 - 1$ (denoting smallness

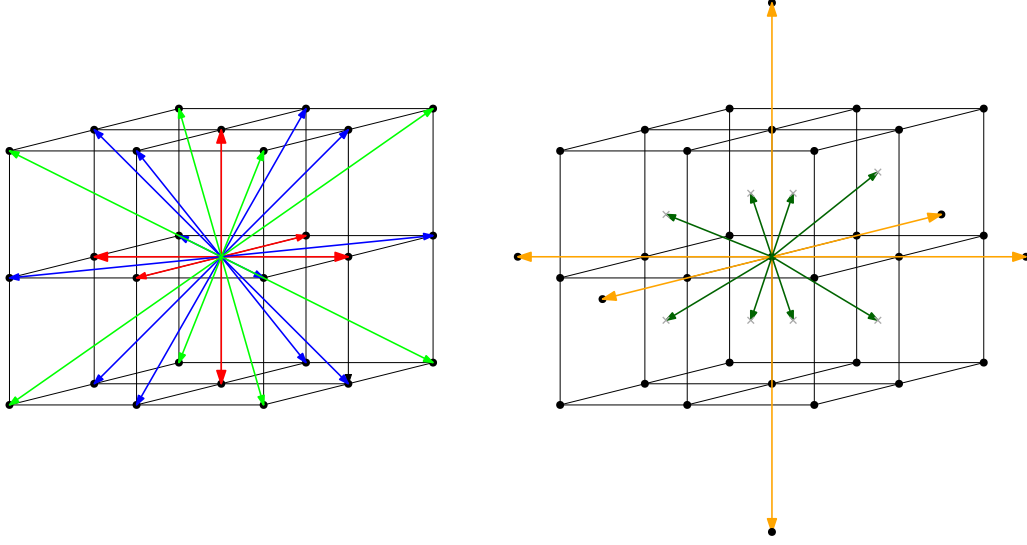


FIG. 3. Energy shells of the $RD3Q41$ model: sc-1(red), fcc-1(blue), bcc-1(light green) shown on a regular lattice and sc-2(orange), bcc- $\frac{1}{2}$ (dark green).

of the temperature deviation). The explicit solution is evaluated up to $O(\eta^3)$ as

$$\tilde{f}_i = w_i \rho \left[1 + \frac{\eta}{2} \left(\frac{c_i^2}{\theta_0} - 3 \right) + \frac{\eta^2}{8} \left(\frac{c_i^4}{\theta_0^2} - 10 \frac{c_i^2}{\theta_0} + 15 \right) + \frac{\eta^3}{48} \left(\frac{c_i^6}{\theta_0^3} - 21 \frac{c_i^4}{\theta_0^2} + 105 \frac{c_i^2}{\theta_0} - 105 \right) \right].$$

The equilibrium distribution at nonzero velocity is derived by expanding the Lagrange multipliers in ϵ (representing smallness of the velocity scale) and the expression for discrete equilibrium accurate up to $O(\epsilon^3)$ is obtained to be

$$f_i^{\text{eq}} = \tilde{f}_i \left\{ 1 + \frac{u_\alpha c_{i\alpha}}{\theta} - \frac{u^2}{2\theta} (1 - A_1) + \frac{1}{2} \left(\frac{u_\alpha c_{i\alpha}}{\theta} \right)^2 + \frac{1}{6} \left(\frac{u_\alpha c_{i\alpha}}{\theta} \right)^3 - \frac{u^2 c_i^2}{6\theta^2} A_1 + \frac{u^2 u_\alpha c_{i\alpha}}{6\theta^2} A_2 - \frac{u^2 c_i^2 u_\alpha c_{i\alpha}}{6\theta^3} A_1 \right\}, \quad (37)$$

where M_2 and M'_2 , the error terms with respect to zero velocity equilibrium moments, and A_1 and A_2

are

$$\begin{aligned} M_2 &= -0.807953 \Delta^3 \theta \left(\frac{\theta_0}{\theta} \right)^2, \\ M'_2 &= -[0.520459 \Delta^2 \theta + 1.41017 \Delta^3 \theta] \left(\frac{\theta_0}{\theta} \right)^2, \\ A_1 &= \frac{5/2M_2}{1 + 5/2M_2}, \\ A_2 &= 5A_1(1 - M_2) - (3 + M'_2 - 5M_2), \end{aligned} \quad (38)$$

with $\Delta\theta = \theta - \theta_0$. The equilibrium moments for this model are

$$\begin{aligned} P_{\alpha\beta}^{\text{eq}} &= \rho\theta\delta_{\alpha\beta} + \rho u_\alpha u_\beta (1 - M'_2) \\ &+ \frac{u^2}{2} \delta_{\alpha\beta} \left[4M'_2 - 5M_2 - \frac{\frac{5}{3}M_2 + \frac{25}{6}M_2^2}{1 + \frac{5}{2}M_2} \right], \\ q_\alpha^{\text{eq}} &= 5\theta u_\alpha (1 - M_2) + \frac{1}{6} u^2 u_\alpha \left[5A_2(1 - M_2) \right. \\ &\left. - 7A_1(1 - M_3) + 7(3 + 2M'_3 - 5M_3) \right], \end{aligned}$$

TABLE I. Energy shells and their corresponding velocities with weights for $RD3Q41$.

Shells	Discrete velocities (c_i)	Weight (w_i)
0	(0, 0, 0)	0.1975697820320461
sc-1	($\pm 1, 0, 0$), ($0, \pm 1, 0$), ($0, 0, \pm 1$)	0.04743040745116578
sc-2	($\pm 2, 0, 0$), ($0, \pm 2, 0$), ($0, 0, \pm 2$)	0.00165687664501576
fcc-1	($\pm 1, \pm 1, 0$), ($\pm 1, 0, \pm 1$), ($0, \pm 1, \pm 1$)	0.00651175327832464
bcc-1	($\pm 1, \pm 1, \pm 1$)	0.00454087801154440
bcc- $\frac{1}{2}$	($\pm 0.5, \pm 0.5, \pm 0.5$)	0.04917980624482672

$$\begin{aligned}
R_{\alpha\beta}^{\text{eq}} &= 5\theta^2\delta_{\alpha\beta}(1 - M_3) \\
&\quad - \frac{5u^2\theta}{2}\delta_{\alpha\beta}\frac{1}{1 + \frac{5}{2}M_2} \\
&\quad - \frac{35u^2\theta}{6}\delta_{\alpha\beta}\left(1 - \frac{1}{1 + \frac{5}{2}M_2}\right) \\
&\quad + \frac{7u^2\theta}{2}\delta_{\alpha\beta}(1 + 4M'_3 - 5M_3) \\
&\quad + 7u_\alpha u_\beta \theta(1 - M'_3),
\end{aligned} \tag{39}$$

where

$$\begin{aligned}
M_3 &= - [0.69253\Delta^2\theta - 2.49925\Delta^2\theta]\left(\frac{\theta_0}{\theta}\right)^3, \\
M'_3 &= -3.18168\left(\frac{\theta_0}{\theta}\right)^3 \\
&\quad \times (0.0934743\Delta\theta + 0.636954\Delta^2\theta + \Delta^3\theta).
\end{aligned} \tag{40}$$

The $P_{\alpha\beta}^{\text{eq}}$, q_α^{eq} , and $R_{\alpha\beta}^{\text{eq}}$ moments of the equilibrium distribution have errors of the order $O(u^2\eta^2)$, $O(u\eta^3)$, and $O(\eta^2)$, respectively, and match with the moments of the Maxwell-Boltzmann distribution up to high accuracy. Thus, model accurately recovers linearized Navier-Stokes-Fourier hydrodynamics.

In the upcoming sections, we validate the accuracy and robustness of the proposed $RD3Q41$ model by simulating various canonical flows related to acoustics, compressible, turbulent, multiphase, and thermal flows.

VI. ACOUSTICS

In the previous sections, the $RD3Q41$ model has been shown to recover the full Navier-Stokes-Fourier equations as its macroscopic limit. In this section, we select a few well-studied benchmarking problems related to the propagation of an acoustic pulse.

As a first example, we present an isothermal simulation of propagation of a two-dimensional (2D) acoustic pulse. The third direction has two lattice points, and periodic boundary conditions are imposed. An axisymmetric density pulse is initialized at the center of a uniform fluid of size $[-1, 1]$ in both x and y directions as

$$\rho(x, y, t = 0) = \rho_0[1.0 + \rho'(x, y, t = 0)], \tag{41}$$

where

$$\begin{aligned}
\rho'(x, y, t = 0) &= \epsilon e^{-\alpha r^2}, \quad \epsilon = 0.001, \quad \alpha = \frac{\ln(2)}{b^2}, \\
b &= 0.1, \quad r = \sqrt{x^2 + y^2}.
\end{aligned} \tag{42}$$

A small value of ϵ is chosen to keep the amplitude of the acoustic perturbation small. For low amplitudes of density fluctuations and low viscosity, the exact solution of the density fluctuation is given by the analytical solution of the linearized Euler equations [53,54] as

$$\rho'(x, y, t) = \rho_0 \times \frac{\epsilon}{2\alpha} \int_0^\infty \exp\left(\frac{-\xi^2}{4\alpha}\right) \cos(c_s \xi t) J_0(\xi r) \xi d\xi, \tag{43}$$

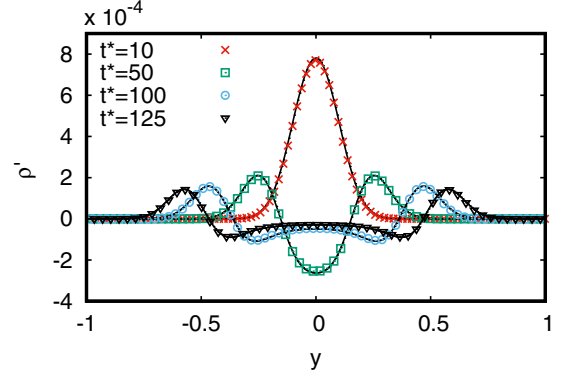


FIG. 4. Density fluctuations along the center line in isothermal case (solid line) at different time steps compared with analytical solution (points).

where J_0 is the Bessel function of the first kind of zero order [55].

An excellent match is observed upon comparing density fluctuations along the centerline from isothermal simulation using our model and from the analytical solution at various time steps (t^*) as shown in Fig. 4. This confirms that the linearized acoustics are captured accurately in an isothermal setting.

To show that the ratio of sound speeds in a thermal to isothermal model is $\sqrt{\gamma}$, we perform thermal simulation of the same setup and compare the pressure fluctuations at times (t^*) with that obtained from an isothermal simulation at times $t = \sqrt{\gamma} \times t^*$. The specific heat ratio γ for the current model is $5/3$. The pressure fluctuation p' is defined as the deviation of pressure from rest condition as $p' = p - \rho_0\theta_0$. It can be seen from Fig. 5 that the profiles match very well, confirming that the ratio of speed of sound is $\sqrt{\gamma}$ and energy conserving LB model indeed recovers the correct isentropic sound speed.

A. 3D acoustic spherical pulse source

We demonstrate the utility of the present model in three dimensions (3D) via a simulation of a spherical pulse source. An acoustic pulse is initialized in the center of the domain of size $[-1, 1]$ in x , y , and z directions as

$$\rho(x, y, z, t = 0) = \rho_0[1.0 + \rho'(x, y, z, t = 0)], \tag{44}$$

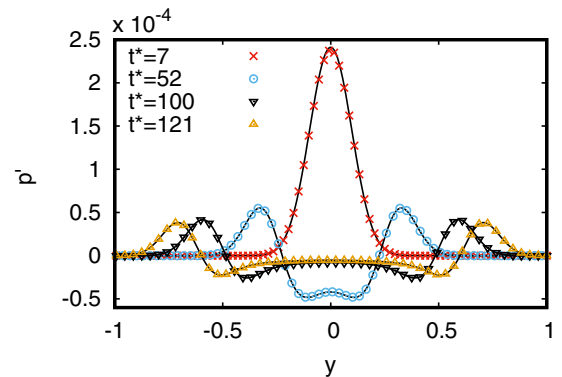


FIG. 5. Comparison of pressure fluctuations along the center line at time t^* from a thermal simulation (solid line) and isothermal simulation (points) at time $\sqrt{\gamma} \times t^*$.

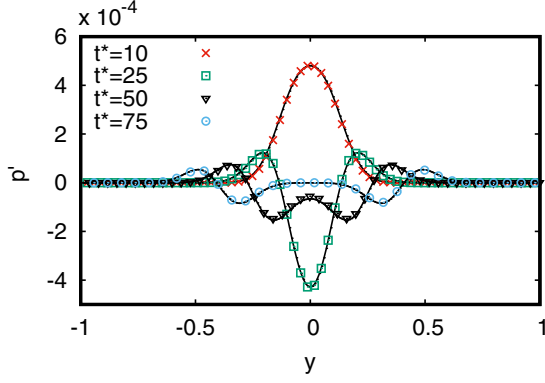


FIG. 6. Density fluctuations due to a 3D spherical pulse source along the y axis at $(x, z) = (0.5, 0.5)$ from LB simulation (line) and exact solution (points).

where

$$\rho'(x, y, z, t = 0) = \epsilon e^{-\alpha r^2}, \quad \epsilon = 0.001, \quad \alpha = \frac{\ln(2)}{b^2},$$

$$b = 0.03, \quad r = \sqrt{x^2 + y^2 + z^2}. \quad (45)$$

The exact solution for the density fluctuation is given as [56]

$$\rho'(x, y, t) = \frac{\epsilon}{2\alpha\sqrt{\pi\alpha}} \int_0^\infty \exp\left(\frac{-\xi^2}{4\alpha}\right) \frac{\sin(\xi r)}{\xi r} \xi^2 d\xi. \quad (46)$$

The density fluctuations from the LB simulation and the exact solution are plotted at a few time steps (t^*) along the y axis at $(x, z) = (0.5, 0.5)$ in Fig. 6 and they show an excellent agreement.

B. Acoustic pulse reflecting off a planar wall

We now demonstrate the capability of the model to simulate the interaction of acoustic waves with simple boundaries. The interaction of an acoustic wave in a mean flow of Mach number $Ma = 0.5$ with an inviscid planar wall is simulated. A domain of length $[-100L, 100L]$ and $[0, 200L]$ is chosen along the x and y axes. An acoustic pulse is initiated at $t = 0$ as

$$p' = A \exp\left(-\ln(2)\left[\frac{x^2 + (y - 25)^2}{25}\right]\right), \quad (47)$$

with $u = 0.5c_s$, $v = 0$, and $A = 10^{-4}$. This setup is identified as an effective test case to check the wall boundary conditions and an analytical solution for the pressure fluctuations is given in Ref. [57] as

$$p' = \frac{A}{2\alpha} \int_0^\infty \exp\left(\frac{-\xi^2}{4\alpha}\right) \cos(\xi t) [J_0(\xi \eta) + J_0(\xi \zeta)] \xi d\xi, \quad (48)$$

where $\alpha = \ln(2)/25$, $\eta = \sqrt{(x - Ma \times t)^2 + (y - 25)^2}$, and $\zeta = \sqrt{(x + Ma \times t)^2 + (y - 25)^2}$. We choose four lattice points per L for this simulation. Pressure fluctuations normalized with A obtained from the current simulation and the analytical solution after a time of $50t_c$ at $y = 24L$ show an excellent match in Fig. 7. Contours of these normalized pressure fluctuations at the initial time and after $50t_c$ are

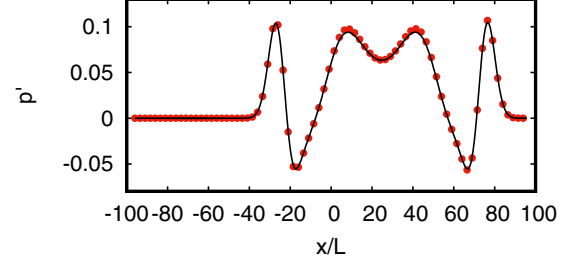


FIG. 7. Pressure fluctuations normalized with A at $y = 24L$ after 50 convection times (LB: line, analytical: points).

shown in Fig. 8. The convection time t_c here is defined as L/c_s .

C. Acoustic scattering off a rigid cylinder

The acoustic scattering off a rigid cylinder is one of the benchmark problems identified as a simplified model to find the sound scattered by aircraft fuselage produced by the propeller [58]. The fuselage was approximated as a circular cylinder and the source of sound reduced to a point source. Presence of a curved boundary also makes this a natural extension to the previous test case for validating the wall boundary conditions.

A cylinder of diameter D_0 is placed at the center of a domain of length $[-15D_0, 15D_0]$ in both x and y directions. At a distance of $4D_0$ from the center of the cylinder along the

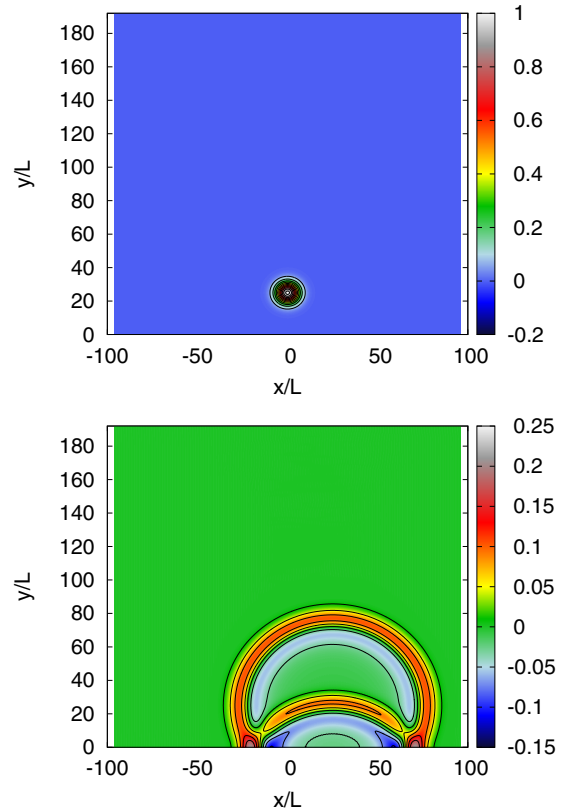


FIG. 8. Contours of pressure fluctuations normalized with A at $t = 0$ (up) and $t = 50$ convection times (bottom).

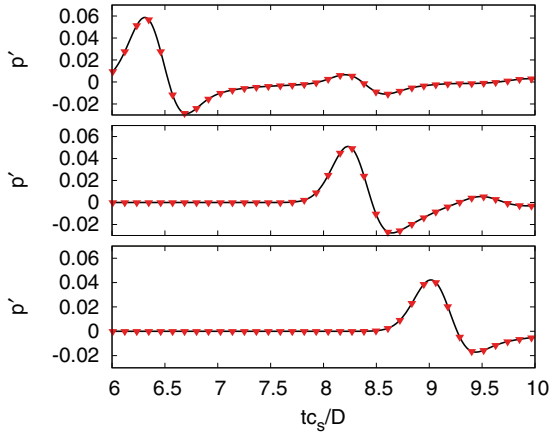


FIG. 9. Time evolution of pressure fluctuations normalized by p_0A at points $r = 5D_0$ and $\theta = 90^\circ, 135^\circ$, and 180° from top to bottom (LBM: solid line, analytical: points).

x axis, a Gaussian acoustic pulse is initialized at $t = 0$ as

$$p' = A \exp\left(-\ln(2)\left[\frac{(x-4)^2 + y^2}{0.2^2}\right]\right), \quad (49)$$

where $A = 10^{-4}$. The analytical solution for this test case is given as [59]

$$p' = \text{Re}\left\{\int_0^\infty [A_i(x, y, \omega) + A_r(x, y, \omega)]\omega e^{-i\omega t} d\omega\right\}. \quad (50)$$

The A_i and A_r stand for the amplitudes of incident and reflected waves given by

$$A_i(x, y, \omega) = \frac{1}{2b} e^{-\omega^2/(4b)} J_0(\omega r_s), \quad (51)$$

where $r_s = \sqrt{(x - 4D_0)^2 + y^2}$, J_0 is Bessel function of zero order, and

$$A_r(x, y, \omega) = \sum_{k=0}^\infty C_k(\omega) H_k^{(1)}(r\omega) \cos(k\theta), \quad (52)$$

with

$$C_k(\omega) = \frac{1}{2\pi} \exp\{-\omega^2/(4b)\} \frac{\epsilon_k}{[H_k^{(1)}]'} \times \int_0^\pi J_1(\omega r_{s0}) \frac{r_0 - 4 \cos(\theta)}{r_{s0}} \cos(k\theta) d\theta,$$

where $\epsilon_0 = 1$, $\epsilon_k = 2$ for $k \neq 0$, $r_0 = \frac{1}{2}$ and $r_{s0} = \sqrt{0.25 + x_s^2 D_0^2 - x_s D_0 \cos(\theta)}$ while $H_k^{(1)}$ is the Hankel function of first order [55].

Pressure fluctuation profiles normalized with p_0A from times $t = 6$ to 10 convection times at three points $A(r = 5D_0, \theta = 90^\circ)$, $B(r = 5D_0, \theta = 135^\circ)$, and $C(r = 5D_0, \theta = 180^\circ)$ are shown in Fig. 9. The convection timescale is defined based on the diameter of the cylinder and speed of sound as D_0/c_s . The points and time interval are chosen such that only the acoustic wave reflected off the cylinder passes

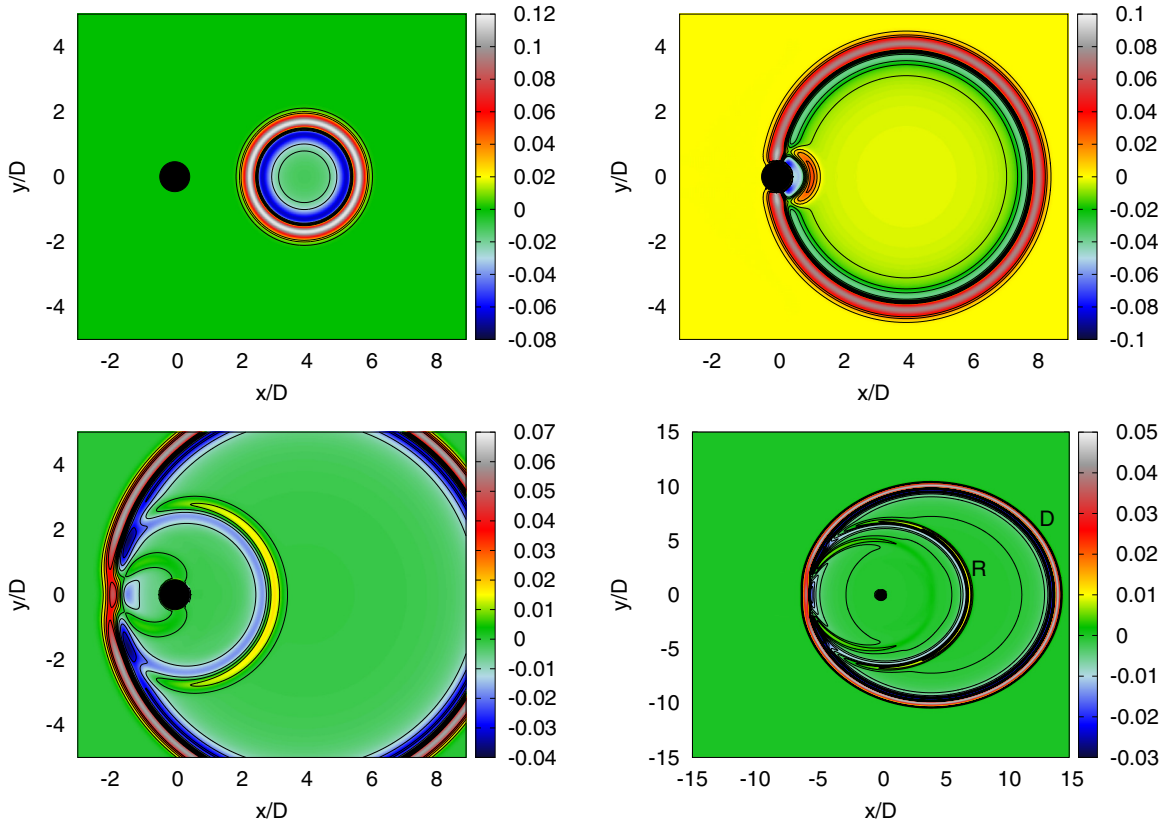


FIG. 10. Isocontours of pressure fluctuations normalized by p_0A at $t = 1.6, 4.0, 6.0$, and 10.0 convection times where D is the direct wave and R is the wave reflected off the surface of the cylinder.

through these points. The pressure fluctuation profiles show a good agreement with the exact solution demonstrating the capability of the current model for solving computational aeroacoustics problems with nontrivial boundary shapes.

Isocontours of pressure fluctuations normalized by p_0A are shown in Fig. 10 at times $t = 1.6, 4.0, 6.0,$ and 10.0 convection times. The contours also show the direct wave D and the acoustic waves reflecting off the surface of the cylinder R .

VII. THERMAL FLOWS

In this section, we demonstrate the efficacy of the *RD3Q41* model for simulating thermal flows by studying two test cases: a Couette flow with a temperature gradient (where the viscous heat dissipation becomes crucial) and heat conduction in a 2D cavity.

A. Viscous heat dissipation

We consider the steady state of flow induced by a wall at $y = H$ moving with a constant horizontal velocity U_0 and maintained at a constant elevated temperature T_1 . The lower wall at $y = 0$ is kept stationary at a constant temperature T_0 ($T_1 > T_0$).

This setup is well suited to validate the effect of viscous heat dissipation. Each layer of fluid drags the layer below it due to friction, which results in the mechanical energy being converted to thermal heating and, therefore, the heat produced affects the temperature profile in bulk. The analytical solution for the temperature profile for this setup is [60]

$$\frac{T - T_0}{\Delta T} = \frac{y}{H} + \frac{Ec}{2} \frac{y}{H} \left(1 - \frac{y}{H}\right), \quad (53)$$

where $\Delta T = T_1 - T_0$ is the temperature difference between the two walls and $Ec = U_0^2 / (c_p \Delta T)$ is the Eckert number that represents the ratio of viscous dissipation to heat conduction with $c_p = \frac{5}{2}$ as the specific heat at constant pressure.

Simulations were performed for $Ec = 0.5, 2.0, 5.0$ with $U_0 = 0.02$ and $\Delta\theta$ calculated according to respective Eckert numbers. The walls were maintained at temperatures $\theta_0 + 0.5\Delta\theta$ and $\theta_0 - 0.5\Delta\theta$. Kinetic boundary conditions as described in Refs. [27,61] have been applied at the walls, and

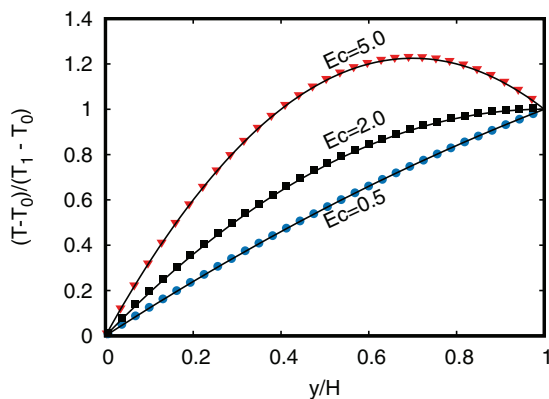


FIG. 11. Mean planar temperature profiles obtained from *RD3Q41* at steady state (symbols) compared to the analytical solution (lines).

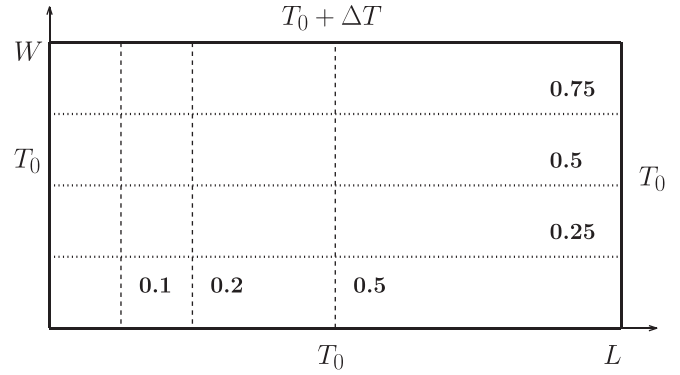


FIG. 12. Setup for the 2D cavity heated at the top.

periodic boundary conditions are used in the other two directions. Figure 11 compares the temperature profiles obtained analytically and via simulations and they are found to agree well.

B. 2D cavity heated at the top

In this setup, the fluid is confined in a rectangular cavity bounded with stationary walls on all four sides. The height of the cavity is W , and its length is L . The top wall is maintained at temperature (T_1), and the other three walls are maintained at temperature T_0 ($T_1 > T_0$) (see Fig. 12). The temperature

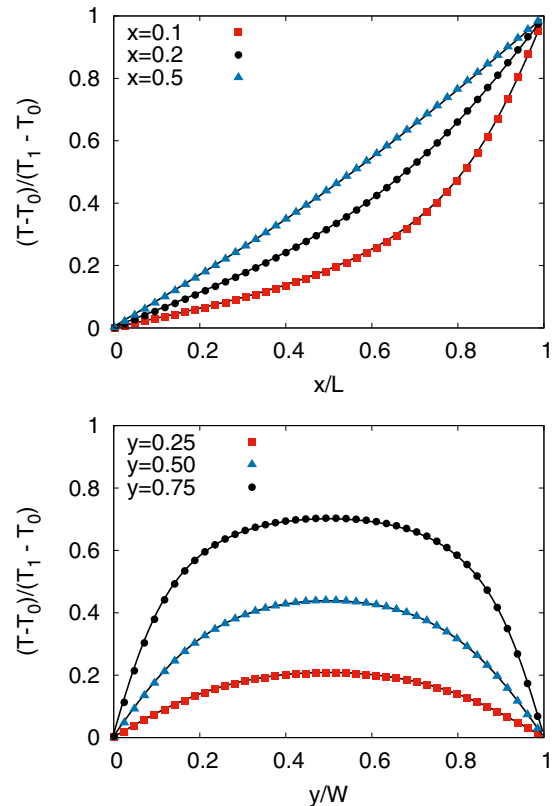


FIG. 13. Steady-state temperature profiles at sections along x axis (left) and y axis (right). The symbols are the solution from the *RD3Q41* model while the lines represent the analytical solution.

profile for this setup at the steady state is given by

$$\frac{T - T_0}{T_1 - T_0} = \frac{2}{\pi} \sum_{n=1}^{\infty} \frac{(-1)^{n+1} + 1}{n} \sin(n\pi x) \frac{\sinh(n\pi y)}{\sinh(n\pi H/L)}. \tag{54}$$

Kinetic boundary conditions as described in Ref. [61] have been applied at the top and bottom walls and periodic boundary conditions are applied in the z direction. The temperature profiles along the constant $x = 0.1, 0.2, 0.5$ and constant $y = 0.25, 0.5, 0.75$ are shown in Fig. 13 and can be seen to match well with the analytical solution.

These two test cases prove that the thermal transport phenomenon is modeled correctly in the *RD3Q41* model.

VIII. THERMOACOUSTICS

In the previous sections, we showed that the current model accurately predicts acoustic and thermal phenomena individually. We now demonstrate the capability of the *RD3Q41* model in simulating flows involving both thermal and acoustic phenomena.

A simple example is when a compressible fluid confined between two walls is heated rapidly on one end, it sets up a convective current [62–64]. The heated wall creates a pressure wave which reflects back and forth in the medium until it gets dissipated by viscosity. These pressure waves are called thermoacoustic waves because of the acoustic nature of the origin of these waves. It is understood that this thermally induced motion is known to enhance the heat transfer in the medium by addition of convective mode to the conductive mode of heat transfer [62]. The convective mode slowly dissipates due to the dissipation of the pressure wave, and conduction becomes the only mode of heat transfer [65]. The many time and length scales present in the system along with the compressible nature of the fluid makes numerical modeling of thermoacoustic convection a challenging problem.

The setup consists of a fluid column of length L enclosed between two walls. It is initially at a uniform temperature of T_0 , as shown in Fig. 14. At times $t > 0$, the bottom wall is maintained at temperature T_0 while the top wall is rapidly heated to a temperature $T_0 + \Delta T$. Kinetic boundary conditions, as described in Ref. [61], have been applied at the walls. The compression and rarefaction of the thermoacoustic waves due to rapid heating create a fluctuating velocity in the domain which results in a significant increase in the rate of heat transfer relative to pure conduction.

The thermoacoustic waves can be predicted by linearized NSF equations too, but the wave speeds predicted are slower

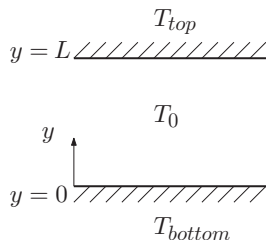


FIG. 14. A schematic of the setup for thermoacoustic convection.

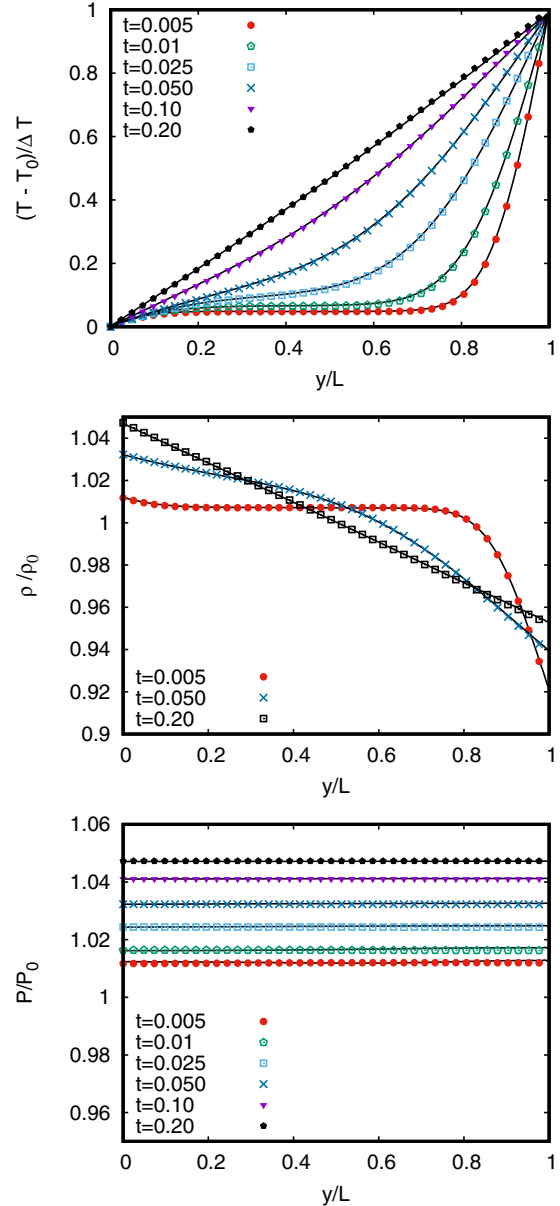


FIG. 15. Nondimensional temperature, density, and pressure at a few intermediate times scaled by diffusion time. (LBM: points; solution of NSF equations: lines).

than the speeds obtained by solving the NSF equations with the nonlinear term included [66]. Navier-Stokes-Fourier (NSF) equations including the nonlinear term are solved as described in Ref. [62] to compare the evolution of the nondimensional temperature, density, and pressure obtained from the *RD3Q41* model at a few intermediate times scaled by diffusion time. Diffusion time is defined as L^2/ν , where ν is kinematic viscosity of the fluid. Results from both the methods are in good agreement, as shown in Fig. 15.

IX. NONIDEAL FLUIDS AND TWO-PHASE FLOW

The standard lattice Boltzmann method leads to an ideal gas equation of state. Several variations to simulate nonideal fluids have been proposed [67–71]. Most of the mentioned

approaches model the microscopic physics and the interfacial dynamics at the mesoscopic level at an affordable computational expense. The LBM is considered advantageous for multiphase flows as it maintains a stable interface and does not require explicit interface tracking. Reference [68] considered the microscopic interactions between the nearest neighbors to model the collision operator for which the surface tension could be maintained automatically [2]. The interaction potential controlled the form of the equation of state of the fluid and gave rise to phase separation, however, the surface tension could not be freely adjusted [72]. Among the various multiphase models, of particular interest is the free-energy model [69] as it allows for surface tension to be independent of the viscosity in addition to being thermodynamically consistent. Recently, the entropic lattice Boltzmann model was extended for multiphase flows to control the spurious currents at the liquid-vapor interface, thereby opening the possibility to simulate large density ratios [43].

At the macroscopic scale, the multiphase LBMs can be considered diffuse interface models. These models smoothen the discontinuity at the interface over a thin but numerically resolvable layer. The fluid properties transition over this layer smoothly as opposed to singular interfaces which have a sharp discontinuity. The surface tension is transformed into a volumetric forcing [73] and is spread over the diffused interfacial region. An undesirable feature of the diffuse interface in LBM manifests in the form of the spurious currents that develop in the vicinity of the interface [72,73]. Several attempts have been made to identify their origin and to alleviate these currents [73,74]. The departure of the LBM simulations from the theoretical phase densities and the magnitude of the spurious current depends upon the liquid-vapor density ratio, the equation of state, and the surface tension. Often they have been attributed to the violation of Gibbs-Duhem equality due to the discrete derivative operator [75]. It was mentioned in Ref. [75] that an open problem in this field is the identification of a discrete derivative operator that preserves the Gibbs-Duhem equality at the interface.

The *RD3Q41* lattice is expected to offer an edge over the conventional lattices because of the presence of the bcc grid points that allow the derivatives to be calculated more accurately. In this section, we propose an alternate way of treating the discrete derivative such that the violation of Gibbs-Duhem relation at the interface is reduced. We show that this way of discretization leads to accurate liquid vapor phase densities and reduces the spurious currents. We first review the van der Waals theory of a single component two-phase fluid followed by the equations of hydrodynamics and the methodology to incorporate nonideal effects in the kinetic theory and lattice Boltzmann model. It is followed by expressions for evaluating second- and fourth-order accurate derivatives on a lattice and the justification of the choice of stencil employed to evaluate derivatives. We then propose a discrete derivative operator to reduce the spurious currents. To prove the thermodynamic consistency, we choose an equation of state and compare densities obtained from a deeply quenched liquid-vapor system with their corresponding theoretical values. Finally, we extend the entropic formulation of LBM to two-phase flows and simulate a head-on collision between two droplets.

In this section, we consider an isothermal system of a nonideal fluid. Van der Waals modified the free-energy density by incorporating terms that are large only when the density gradients are significant [76,77]. Therefore, the underlying free-energy functional $\Psi(x)$ is of the form

$$\Psi(x) = \int [\mathcal{F}(\rho(x)) + \mathcal{I}(\nabla\rho(x), \nabla^2\rho(x), \dots)] dx, \quad (55)$$

where ρ is the density, \mathcal{F} is the bulk free energy, and \mathcal{I} is the interfacial free energy. The interfacial free energy $\mathcal{I}(\nabla\rho(x), \nabla^2\rho(x), \dots)$ is approximated to the lowest order as [75,77]

$$\mathcal{I}(\nabla\rho(x), \nabla^2\rho(x), \dots) = \frac{\kappa(\rho)}{2} |\nabla\rho(x)|^2. \quad (56)$$

For simplicity, $\kappa(\rho)$, related to the surface tension, is taken constant. With this definition, the excess free energy is the surface tension σ :

$$\sigma = \int_{-\infty}^{\infty} \frac{\kappa}{2} |\nabla\rho(x)|^2 dx. \quad (57)$$

The above model of free energy is the simplest model that gives two stable phases provided \mathcal{F} has two minima and was first formulated by van der Waals [76].

The macroscopic mass and momentum conservation equations are given by [78,79]

$$\partial_t \rho + \partial_\alpha (\rho u_\alpha) = 0, \quad (58)$$

$$\partial_t (\rho u_\alpha) + \partial_\beta [p \delta_{\alpha\beta} + \rho u_\alpha u_\beta + \sigma_{\alpha\beta} + \sigma_{\alpha\beta}^{(\kappa)}] = 0, \quad (59)$$

where $\sigma_{\alpha\beta}$ is the viscous stress tensor

$$\sigma_{\alpha\beta} = -\rho\nu(\partial_\beta u_\alpha + \partial_\alpha u_\beta) + \frac{2}{3}\rho\nu\partial_\gamma u_\gamma \delta_{\alpha\beta}, \quad (60)$$

where ν is the kinematic viscosity, and $\sigma_{\alpha\beta}^{(\kappa)}$ takes the form

$$\sigma_{\alpha\beta}^{(\kappa)} = \kappa \left[\left(-\frac{1}{2} \partial_\gamma \rho \partial_\gamma \rho - \rho \partial^2 \rho \right) \delta_{\alpha\beta} + \{ \partial_\alpha \rho \partial_\beta \rho \} \right] \quad (61)$$

and accounts for the interfacial stresses. The term within the curly braces in the above expression is known as the van der Waals stress [77].

The nonlocal pressure tensor (also known as Korteweg's stress tensor) derived from the above description is consistent with the definition of the free-energy functional and is written as [69,80,81]

$$P_{\alpha\beta} = \left[p - \frac{\kappa}{2} \partial_\gamma \rho \partial_\gamma \rho - \kappa \rho \partial^2 \rho \right] \delta_{\alpha\beta} + \kappa \partial_\alpha \rho \partial_\beta \rho, \quad (62)$$

where $\delta_{\alpha\beta}$ is the Kronecker delta and

$$p = \rho\mu_0 - \mathcal{F} \quad (63)$$

is the equation of state describing the nonideal fluid, with $\mu_0 = \partial\mathcal{F}/\partial\rho$ as the bulk chemical potential. For a continuous system, the Gibbs-Duhem equality is trivially satisfied. However, it gets violated for a discrete system due to the definition of the discrete derivative which leads to thermodynamic inconsistency [75].

To incorporate the deviation from the ideal gas the intermolecular attraction, the repulsion between the particles due to their nonvanishing size, and the interface dynamics needs to be modeled. In LBM framework, the attractive and repulsive parts are added as a force term. In order to do so, one begins

with the Boltzmann BGK equation for an isothermal nonideal gas [70]

$$\frac{\partial f_i}{\partial t} + c_{i\alpha} \frac{\partial f_i}{\partial x_\alpha} = \frac{f_i^{\text{eq}}(\rho, \mathbf{u}, \theta_0) - f_i}{\tau} + F_i, \quad (64)$$

where the forcing term F_i is given by

$$F_i = \frac{g_\alpha^{\text{nid}}(c_{i\alpha} - u_\alpha)}{\theta_0} f_i^{\text{eq}}(\rho, \mathbf{u}, \theta_0). \quad (65)$$

The nonideal contributions are captured in g_α^{nid} :

$$g_\alpha^{\text{nid}} = -\frac{1}{\rho} \partial_\beta P_{\alpha\beta}^{\text{nid}}, \quad P_{\alpha\beta}^{\text{nid}} = P_{\alpha\beta} - \rho \theta_0 \delta_{\alpha\beta}. \quad (66)$$

The above form of g_α^{nid} , known as the pressure formulation, is sufficient to incorporate the nonideal interactions and the Korteweg's stress tensor in the lattice Boltzmann model [43,73,78]. Alternatively, by exploiting the Gibbs-Duhem relation, one can write the chemical potential formulation as [73,79]

$$g_\alpha^{\text{nid}} = -\partial_\alpha \mu^{\text{nid}}, \quad (67)$$

where $\mu^{\text{nid}} = \mu_0^{\text{nid}} - \kappa \partial^2 \rho$.

Equation (64) is integrated along the characteristics using the trapezoid rule to obtain the discrete (in space and time) evolution of populations as

$$\begin{aligned} \tilde{f}_i(\mathbf{x} + \mathbf{c}_i \Delta t, t + \Delta t) &= \tilde{f}_i(\mathbf{x}, t) + \alpha \beta [f_i^{\text{eq}}(\rho, \mathbf{u}, \theta_0) \\ &\quad - \tilde{f}_i(\mathbf{x}, t)] + \left(1 - \frac{\alpha \beta}{2}\right) \Delta t F_i, \end{aligned} \quad (68)$$

where \tilde{f}_i is a transformation of the populations f_i defined as

$$\tilde{f}_i = f_i - \frac{\Delta t}{2\tau} [f_i^{\text{eq}}(\rho, \mathbf{u}, \theta_0) - f_i] - \frac{\Delta t}{2} F_i, \quad (69)$$

$\beta = \Delta t / (2\tau + \Delta t)$, and $\alpha = 2$ for the standard LBM. For the entropic LBM the parameter α needs to be computed such that the dynamics obeys the H theorem. The macroscopic variables are calculated as

$$\rho = \sum_i \tilde{f}_i, \quad u_\alpha = \frac{1}{\rho} \sum_i \tilde{f}_i c_{i\alpha} + \frac{\Delta t}{2} g_\alpha^{\text{nid}}. \quad (70)$$

It is worth noticing that Eq. (68) does not conserve momentum. The change in momentum at each site during a time step is obtained by multiplying Eq. (68) with $c_{i\alpha}$ and summing over all directions as

$$\rho u_\alpha(t + \Delta t) - \rho u_\alpha(t) = \Delta t \rho g_\alpha^{\text{nid}}. \quad (71)$$

In fact, this change in momentum is due to the nonideal nature of the fluid and leads to two stable phases separated by an interface. However, the global momentum of the system should be exactly conserved provided no net momentum exchange occurs at the boundary [68]. This is an important feature of the discrete dynamics, satisfied by the pressure formulation [Eq. (66)] but not by the chemical potential formulation [Eq. (67)]. It is known that the chemical potential formulation is more accurate than the pressure formulation and leads to smaller spurious currents [73,79]. However, the thermodynamic consistency requires that the global momentum should

stay preserved. This will be elaborated in the forthcoming sections, where we propose an alternate formulation that is similar to the chemical potential formulation but preserves global momentum.

A. Discretization scheme

As discussed earlier, for a continuous system the Gibbs-Duhem relation is trivially satisfied. However, for a discrete system it gets violated, i.e.,

$$\tilde{\partial}_\alpha P_{\alpha\beta} \neq \rho \tilde{\partial}_\beta \mu, \quad (72)$$

where $\tilde{\partial}_\alpha$ represents the discrete derivative operator [75]. This is the reason why the two formulations, namely, the pressure and the chemical potential, show different accuracy, stability, and spurious currents.

The chemical potential formulation is more accurate and has smaller spurious currents as compared to the pressure formulation [73]. However, one of its drawbacks is that the global momentum is not conserved. This is further explained in what follows: In the pressure formulation in 1D, the second-order discrete derivative $\tilde{\partial}_\alpha^{(2)}$ at the n th grid point is written as

$$\tilde{\partial}_\alpha^{(2)} P_{\alpha\beta} = \frac{1}{2\Delta x_\alpha} [P_{\alpha\beta}(n+1) - P_{\alpha\beta}(n-1)]. \quad (73)$$

With appropriate boundary conditions (say periodic), one can sum over the entire domain to show that

$$\sum_{n=1}^N [P_{\alpha\beta}(n+1) - P_{\alpha\beta}(n-1)] = 0. \quad (74)$$

The local change of momentum from Eq. (71) is $\Delta t \rho g_\alpha^{\text{nid}}$. The global momentum conservation upon using Eqs. (66), (73), and (74) follows as

$$\begin{aligned} \sum_{n=1}^N \Delta t \rho g_\alpha^{\text{nid}} &= -\sum_{n=1}^N \Delta t \tilde{\partial}_\alpha^{(2)} P_{\alpha\beta}^{\text{nid}} \\ &= -\frac{\Delta t}{2\Delta x_\alpha} \sum_{n=1}^N [P_{\alpha\beta}^{\text{nid}}(n+1) - P_{\alpha\beta}^{\text{nid}}(n-1)] = 0. \end{aligned} \quad (75)$$

However, for the chemical potential formulation the net global momentum is

$$\sum_{n=1}^N \Delta t \rho g_\alpha^{\text{nid}} = -\frac{\Delta t}{2\Delta x_\alpha} \sum_{n=1}^N \rho(n) [\mu^{\text{nid}}(n+1) - \mu^{\text{nid}}(n-1)], \quad (76)$$

which is nonzero.

Fundamentally, this lack of momentum conservation is emerging due to the violation of the Leibniz rule. For this analysis we ignore the interfacial terms which are added separately. The bulk nonideal pressure using the thermodynamic relations is written as

$$p^{\text{nid}} = \mu_0^{\text{nid}} \rho - \mathcal{F}^{\text{nid}}. \quad (77)$$

Taking the discrete derivative of the above equation one obtains

$$\tilde{\partial}_\alpha p^{\text{nid}} = \{\mu_0^{\text{nid}} \tilde{\partial}_\alpha \rho\} + \rho \tilde{\partial}_\alpha \mu^{\text{nid}} - \tilde{\partial}_\alpha \mathcal{F}^{\text{nid}}, \quad (78)$$

TABLE II. Discretization scheme and the maximum magnitude of spurious current for Peng-Robinson (PR) and Carnahan-Starling (CS) EOS on a grid of size $80 \times 80 \times 4$ at $\theta/\theta_c = 0.9$ using the *RD3Q41* model.

g_α^{nid}	PR [Eq. (83)]	CS
Pressure	6.376×10^{-3}	4.317×10^{-3}
Chemical potential	5.139×10^{-3}	4.281×10^{-3}
Current, $\eta = 1.0$	4.765×10^{-3}	5.565×10^{-3}
Current, $\eta = 0.5$	2.790×10^{-3}	3.706×10^{-3}

where the left-hand side is the pressure formulation which conserves the global momentum. The term in curly braces on the right-hand side is the chemical potential formulation which does not conserve the global momentum because the other two terms (although they cancel in the continuous case) are ignored in the discrete chemical potential formulation. It is interesting to note that if one defines the discrete derivative as

$$\tilde{\partial}_\alpha(AB) = A\tilde{\partial}_\alpha B + B\tilde{\partial}_\alpha A, \quad (79)$$

A, B being arbitrary functions, the Leibniz rule as well as the global momentum conservation holds.

Therefore, the global momentum conserving new formulation using Eq. (78) is written as

$$\rho g_\alpha^{\text{nid}} = -[\rho \tilde{\partial}_\alpha^{(2)} \mu_0^{\text{nid}} + \mu_0^{\text{nid}} \tilde{\partial}_\alpha^{(2)} \rho - \tilde{\partial}_\alpha^{(2)} \mathcal{F}^{\text{nid}} + \kappa \tilde{\partial}_\beta^{(2)} I_{\alpha\beta}], \quad (80)$$

where the interfacial stresses $I_{\alpha\beta}$ are given by

$$I_{\alpha\beta} = [-\frac{1}{2} \partial_\gamma \rho \partial_\gamma \rho - \rho \partial^2 \rho] \delta_{\alpha\beta} + \partial_\alpha \rho \partial_\beta \rho. \quad (81)$$

Ideally, one would prefer to work with the fourth-order discrete derivatives [Eq. (A5)] but they lead to violation of the global momentum conservation. One can, however, use the fourth-order discrete derivative for $\tilde{\partial}_\alpha \mathcal{F}^{\text{nid}}$, for which we use a convex combination of the second- and fourth-order discrete derivative (see Appendix for details). This brings us to the final form of g_α^{nid} :

$$\rho g_\alpha^{\text{nid}} = -[\rho \tilde{\partial}_\alpha^{(2)} \mu_0^{\text{nid}} + \mu_0^{\text{nid}} \tilde{\partial}_\alpha^{(2)} \rho - \eta \tilde{\partial}_\alpha^{(2)} \mathcal{F}^{\text{nid}} - (1 - \eta) \tilde{\partial}_\alpha^{(4)} \mathcal{F}^{\text{nid}} + \kappa \tilde{\partial}_\beta^{(2)} I_{\alpha\beta}]. \quad (82)$$

The above route to calculating the discrete derivative is thermodynamically consistent, preserves the global momentum, and has a parameter $\eta \in [0, 1]$ that can be fine tuned to improve the accuracy, but for this work we restrict ourselves to $\eta = \frac{1}{2}$.

To demonstrate the accuracy of the present model, we simulate a one-dimensional interface of a van der Waals fluid on a grid of size $192 \times 4 \times 4$ using the *RD3Q41* model. Figure 16 shows the densities from the pressure formulation, chemical potential formulation, and the current scheme for three η values. It is evident that the current scheme predicts the values of phase density that match with the theoretical Maxwell's construction values. From Fig. 17 and Table II, it can be seen the maximum magnitude of the spurious current is also reduced upon using the current formulation. Here, it should be pointed out that although $\eta = 0$ gives smaller spurious

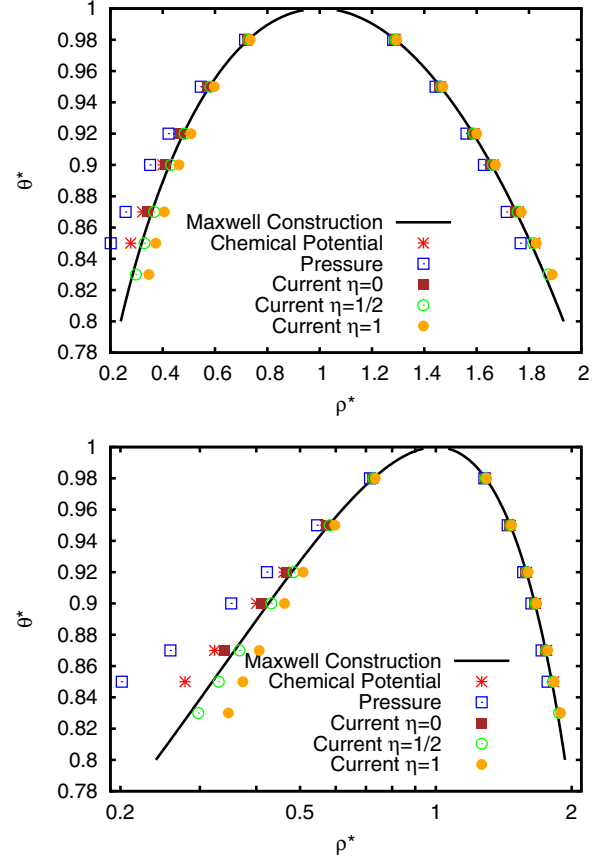


FIG. 16. Liquid vapor densities of the van der Waals fluid for various formulations at different reduced temperature $\theta^* = \theta/\theta_c$. The same plot is represented on the linear scale (top) and the logarithmic scale (bottom) to emphasize the error in density of the gas phase.

currents than $\eta = \frac{1}{2}$, it succumbs to numerical instabilities at a higher $\theta/\theta_c = 0.87$.

B. Sound propagation in a nonideal gas

In this section, we validate the proposed model for sound propagation in an isothermal nonideal gas. For a gas following

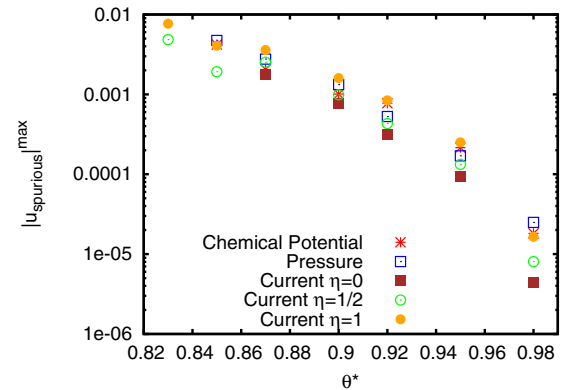


FIG. 17. Spurious currents of the van der Waals fluid for various formulations at different reduced temperature $\theta^* = \theta/\theta_c$.

an ideal equation of state (EOS) $p = \rho\theta_0$ the sound speed is fixed at $\sqrt{\theta_0}$ where θ_0 is a reference temperature. However, in real gases, the speed of sound becomes dependent on the phase density too as pressure is a nontrivial function of phase density. To confirm this, we introduce a density perturbation at constant temperature in a nonideal fluid with Peng-Robinson type equation of state given by

$$p = \rho\theta_0 \frac{1 + \eta + \eta^2 - \eta^3}{(1 - \eta)^3} - \frac{a\rho^2}{1 + 2\rho b - \rho^2 b^2}, \quad (83)$$

where $a = 1.851427622\theta_c/\rho_c$, $b = 0.353748714/\rho_c$ are van der Waals type critical parameters and $\eta = \rho b/4$. Here, θ_c and ρ_c are critical temperature and critical density, respectively.

We compute the speed of sound at various values of θ^* = θ/θ_c and their corresponding equilibrium phase densities (ρ_{ph}) by initializing a 1D density fluctuation of the form

$$\rho(x, t = 0) = \rho_{\text{ph}}[1.0 + \epsilon \cos(\pi x)], \quad (84)$$

in domain of size $[-\pi, \pi]$ in the x direction. The domain has two lattice points in the y and z directions and periodic boundary conditions are applied in all three directions. The wave is expected to reach the same configuration as the initial condition after one wave period (t_p). We track the l2-norm of the density fluctuation computed using the present state and initial state, which is minimum when the waves are in phase after completing one cycle. The domain size (L) and the time period at which l2-norm is minimum are used to compute the speed of sound ($c_s = L/t_p$).

We observe a good agreement with the theoretical prediction of the sound speed in both the phases for a broad range of θ^* as shown in Fig. 18.

C. Quenching of a liquid-gas system

Quenching of a liquid-gas system exhibits phase separation and has been widely accepted as a test for thermodynamic consistency and stability of a multiphase lattice Boltzmann model [82]. We use the Peng-Robinson EOS as defined in Eq. (83), and the Carnahan-Starling EOS. For $\theta < \theta_c$ the system shows phase separations where in the initial stages tiny bubbles of the liquid phase surrounded by the ambient gaseous phase are formed. As time progresses, the bubbles merge to form a stable lamellar film, a cylinder or a spherical droplet. Figure 19 shows the liquid and gas density obtained from the *RD3Q41* model compared against the theoretical values obtained from Maxwell's equal area construction. The model accurately recovers liquid-gas bulk densities, hence is confirmed to be thermodynamically consistent.

D. Droplet collision

We employ the proposed multiphase model and the Carnahan-Starling EOS [83] to simulate binary droplet collision as it offers interesting outcomes depending upon the control parameters [43]. Three particular outcomes observed upon collision at various Reynolds number, Weber number, and the impact parameter are coalescence, stretching separation, and reflexive separation [84].

The setup consists of a rectangular box of $160 \times 200 \times 200$ lattice units with two liquid phase droplets of diameter

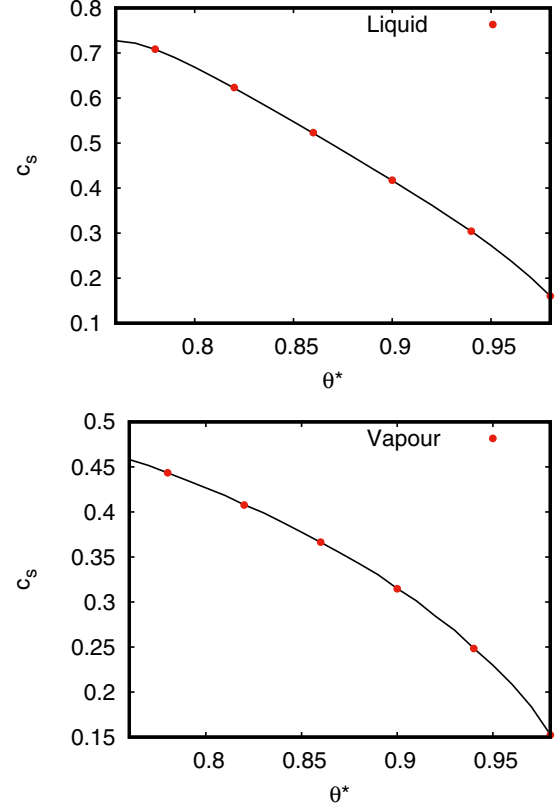


FIG. 18. Speed of sound in a nonideal gas for liquid and vapor phases: theoretical prediction (solid line) and simulation (points).

$D_0 = 45$ units and interface width 5 units located in the ambient of gas phase with a distance of 30 units between their centers. At $t = 0$, they are imparted a relative velocity $U_0 = 0.2$ toward each other. The liquid phase having a density of $\rho_{\text{liq}}/\rho_c = 2.412$ is in equilibrium with the gas phase of density $\rho_{\text{gas}}/\rho_c = 0.185$ at $\theta/\theta_c = 0.8$. The chosen value of $\kappa = 0.001a\Delta x^2$ corresponds to a surface tension $\sigma = 0.223$ when $\Delta x = 1$. The kinematic viscosity of the liquid phase $\nu_{\text{liq}} = 0.0303$, hence, Reynolds number (Re) and the Weber number (We) can be calculated as

$$\text{Re} = \frac{U_0 D_0}{\nu_{\text{liq}}} = 297.03, \quad \text{We} = \frac{\rho_{\text{liq}} U_0^2 D_0}{\sigma} = 19.47. \quad (85)$$

For calculating α required for the entropic formulation of LBM, we rewrite Eq. (68) as

$$\tilde{f}_i(\mathbf{x} + \mathbf{c}_i \Delta t, t + \Delta t) = \hat{f}_i(\mathbf{x}, t) + \alpha \beta [\hat{f}_i^{\text{eq}}(\rho, \mathbf{u}, \theta_0) - \hat{f}_i(\mathbf{x}, t)], \quad (86)$$

where we have the transformations $\hat{f}_i = \tilde{f}_i + \Delta t F_i$ and $\hat{f}_i^{\text{eq}} = \tilde{f}_i^{\text{eq}} + (\Delta t/2)F_i$ with $\Delta t = 1$. These transformations permit us to define $x_i = \hat{f}_i^{\text{eq}}/\hat{f}_i - 1$ and compute the path length α in the spirit of Refs. [85]. Figure 20 shows head-on collision between two droplets in thermodynamic equilibrium with the ambient.

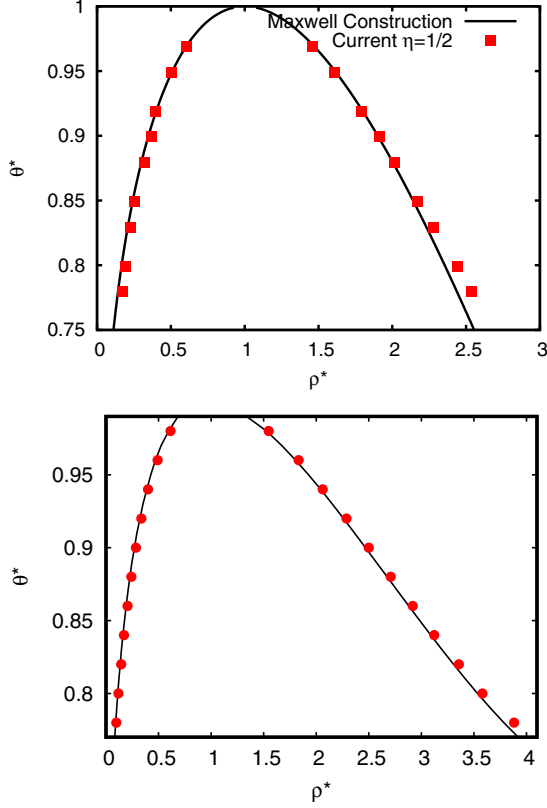


FIG. 19. Equilibrium liquid and gas density $\rho/\rho_c = \rho^*$ obtained from *RD3Q41* model for Carnahan-Starling EOS (top) and Peng-Robinson type EOS (bottom) compared against their respective Maxwell equal area construction at various $\theta/\theta_c = \theta^*$.

X. TURBULENT FLOWS

Higher-order isothermal lattice Boltzmann methods are known to be stable and have been proposed as an alternative to direct numerical simulations (DNS) for fluid turbulence [40]. It is shown that energy conserving LB models are more numerically stable than their non-energy-conserving counterparts [20]. The proposed *RD3Q41* model, which is an energy conserving higher-order LB model, takes advantage of these two features and is a viable alternative for DNS

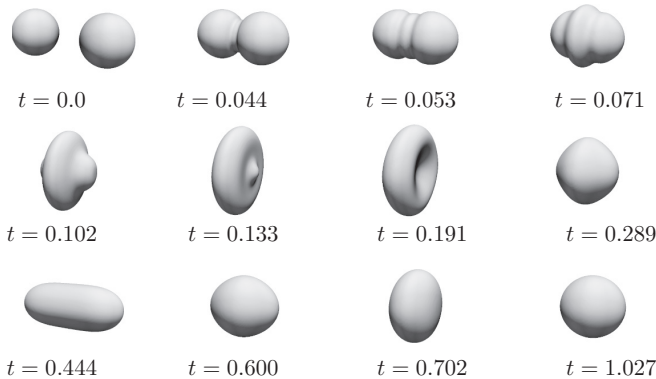


FIG. 20. Head-on collision between two droplets at $Re = 297.03$ and $We = 19.47$.

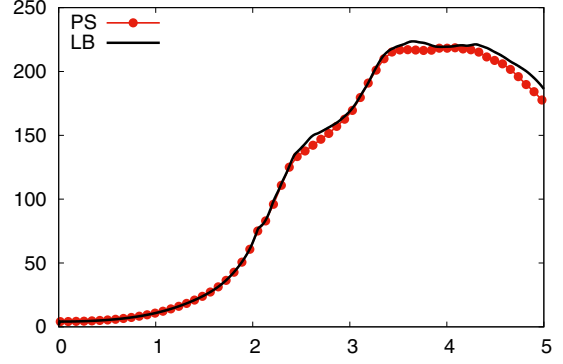


FIG. 21. Comparison of evolution of mean entrophy with time (line: LBM, points: PS).

simulations of turbulent flows. In this section, we present simulations of turbulent flows for three cases: a fully periodic test case of decaying turbulence, flow in a rectangular channel, and flow over a sphere.

A. Kida-Peltz flow

Kida-Peltz flow is a periodic flow with highly symmetric initial conditions and is a good test case for the computational study of high Reynolds number (Re) flows [86]. The initial conditions for the flow are

$$\begin{aligned} u_x(x, y, z) &= U_0 \sin x [\cos(3y) \cos z - \cos y \cos(3z)], \\ u_y(x, y, z) &= U_0 \sin y [\cos(3z) \cos x - \cos z \cos(3x)], \\ u_z(x, y, z) &= U_0 \sin z [\cos(3x) \cos y - \cos x \cos(3y)], \end{aligned} \quad (87)$$

with $x, y, z \in [0, 2\pi]$. The simulations were performed at a Reynolds number 5000 defined based on the domain length and velocity U_0 . In this flow, entrophy (Ω) increases very sharply in the initial time steps and reaches a maximum value and then decays with time. Mean entrophy is calculated from the symmetric velocity gradient tensor [87]

$$S_{\alpha\beta} = \frac{2}{\rho\theta(2\tau + \Delta t)} \sum_i (f_i - f_i^{eq}) c_{i\alpha} c_{i\beta}, \quad (88)$$

where $\tau = \nu/c_s^2$. We demonstrate the efficiency of the proposed *RD3Q41* model by comparing the evolution of mean

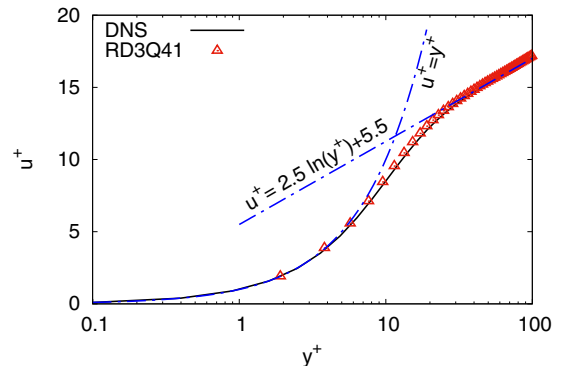


FIG. 22. Mean velocity profiles from our simulation (points) and DNS results (line) from [94].

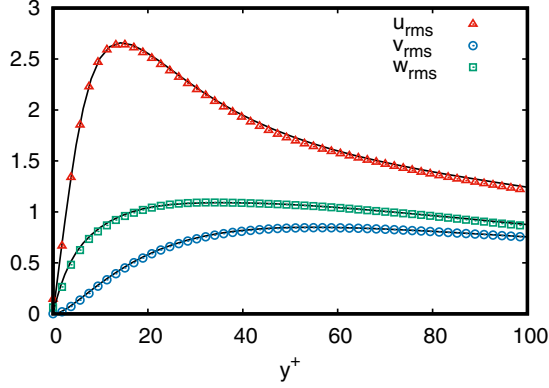


FIG. 23. RMS velocity profiles from our simulation (points) and DNS results (line) from [94].

enstrophy of a Kida-Peltz flow setup with that of pseudospectral (PS) method in Fig. 21.

The pseudospectral method solves the 3D Navier-Stokes (NS) equations in a periodic domain. We use the projection operator $\mathcal{P}_{ij} = \delta_{ij} - k_i k_j / k^2$ to eliminate the pressure term in the Navier-Stokes equations, which allows us to rewrite them in Fourier space as [88]

$$\partial_t [\tilde{u}_j(\mathbf{k}) \exp(vk^2 t)] = \exp(vk^2 t) \mathcal{P}_{ij} F(\mathbf{k}), \quad (89)$$

where $\tilde{u}_j(\mathbf{k})$ denotes velocity in Fourier space, δ_{ij} is the Kronecker delta, $F(\mathbf{k})$ is the Fourier coefficient of the non-linear advection term [87]. Runge-Kutta third-order scheme is used for the time integration and dealiasing of the nonlinear term is performed via the $\frac{2}{3}$ rule [89]. For the MPI (message passing interface) implementation of parallel Fourier transform, FFTW library (version 3), was used which provides a comprehensive collection of fast C routines for computing the discrete Fourier transform [90]. The initial conditions being highly symmetric in space, only odd and even transforms are used, thus reducing the problem size to one eighth (half in each direction) [86], as compared to the full original domain. An in-house solver was used to perform the PS simulations. The numerical implementation of Eq. (89) and details of the solver are given in detail in Ref. [91].

B. Turbulent channel flow

In this section, the proposed $RD3Q41$ model is benchmarked for the classic wall bounded turbulent flow in a rectangular channel. We perform simulations at a friction Reynolds number (Re_τ) ≈ 180 . The friction Reynolds number is defined based on the wall shear velocity (u_τ) and the channel half-width (δ). The simulations were performed a domain of size $12\delta \times 2\delta \times 6\delta$, and the channel half-width was chosen to

TABLE III. Mean flow properties from present $RD3Q41$ simulation and from Ref. [95] at $Re_\tau = 180$.

	C_{f0}	C_f	U_m/u_τ	U_c/u_τ	U_c/U_m
$RD3Q41$	5.95×10^{-3}	8.23×10^{-3}	15.58	18.33	1.17
Ref. [95]	6.04×10^{-3}	8.18×10^{-3}	15.63	18.20	1.16

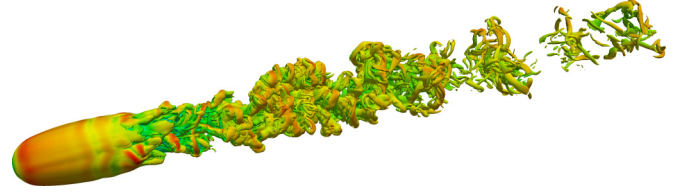


FIG. 24. Isovorticity contours of flow over sphere at Reynolds number = 3700.

be 96 grid points. This corresponds to a nondimensional grid spacing $\Delta x^+ = \Delta x / y^+ \approx 2$ where $y^+ = y u_\tau / \nu$.

The flow is driven by a body force, and periodic boundary conditions are applied in streamwise and spanwise directions. Turbulence in the domain is triggered by adding a divergence-free noise to the initial conditions [92].

At sufficiently high Reynolds numbers in channel flows, the variation of the mean velocity in wall coordinates (u^+) is known to follow the law of the wall [93]. The mean velocity (u^+) scales linearly with wall coordinate y^+ in viscous layer and in the log law region scales as $u^+ = (1/\kappa) \ln(y^+) + B$ where $\kappa = 0.42$ and $B = 5.5$ are constants. Figure 22 shows that the mean flow of velocity in wall coordinates from our simulations follows the law of the wall and is in excellent agreement with that reported in Ref. [94]. RMS velocity profiles also show an excellent agreement, as shown in Fig. 23.

The other mean flow properties like skin friction coefficient (C_f), the ratio of bulk mean velocity (U_m), and center line velocity (U_c) to wall shear velocity (u_τ) show good agreement with Kim *et al.* [95] and are reported in Table III. This shows that the proposed model is well suited to simulate wall bounded turbulent flows.

C. Flow past a sphere

Flow over bluff bodies is a well studied problem that is of considerable academic and practical interest. In this section, we simulate flow past a sphere at Reynolds number of 3700 (see Fig. 24). The Reynolds number is defined based on the free stream velocity U_0 and the diameter of the sphere D_0 . A computational domain of $[-4.725D_0, 15.525D_0] \times [-6.125D_0, 6.125D_0] \times [-6.125D_0, 6.125D_0]$ is used with 80 grid points per diameter of the sphere and the center of sphere located at the origin. The inlet and outlet boundary conditions are based on Ref. [96]. A diffused bounce back boundary condition described in Ref. [97] is implemented on the surface of the sphere. This boundary condition is local in nature, and is implemented in two steps: First, the standard bounce back is applied locally at each grid point,

TABLE IV. Drag coefficient (C_d), average base pressure coefficient (C_p), recirculation length (L_R), separation angle (ϕ_s).

	C_d	Base C_p	L_R	ϕ_s
DNS [98]	0.394	-0.207	2.28	89.4
LES [99]	0.355	-0.194	2.622	90
Experiments [100]		-0.224		
$RD3Q41$	0.427	-0.211	2.241	90

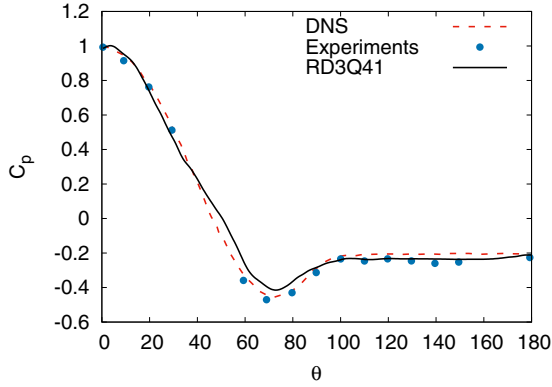


FIG. 25. C_p distribution on the surface of the sphere compared with with the experimental [100] and DNS [98] studies.

after which the density ρ_{boundary} can be calculated since all the populations are known after bounce back. In the second step, the incoming populations are replaced with $f^{\text{eq}}(\rho = \rho_{\text{boundary}}, u_{\text{imposed}}, \theta_{\text{imposed}})$, where $u_{\text{imposed}}, \theta_{\text{imposed}}$ are the velocity and temperature imposed, respectively. Velocity is imposed to be zero on the surface of the sphere and is maintained at constant temperature.

We compare the flow variables such as the drag coefficient, base coefficient pressure, separation angle, and mean recirculation length with the available numerical and experimental data in Table IV. The drag coefficient C_d is defined as

$$C_d = \frac{F_D}{\frac{1}{2}\rho U_0^2 A}, \quad (90)$$

where F_D is the drag force and $A = \pi D_0^2/4$. The recirculation length is defined as the distance between the rear end of the sphere and the location where the velocity in the streamwise direction changes its sign. The angular distribution of the pressure coefficient C_p defined as

$$C_p = \frac{P - P_0}{\frac{1}{2}\rho U_0^2} \quad (91)$$

is plotted over the surface of the sphere in Fig. 25. C_p profiles from an experimental study, and a DNS study are also shown for reference. It is to be noted that capturing the C_p distribution requires a very high resolution of the sphere [101] while with

the current model, we find a reasonable agreement with only 80 points per diameter.

The averaged profile of the velocity in the streamwise direction normalized with the free stream velocity at three different locations ($x/D_0 = 0.2, 1.6, 3.0$) in the wake of the sphere are shown in Fig. 26. The averaged profiles of the flow show a good agreement with the DNS [98], LES [99], and experimental [100] studies.

XI. OUTLOOK

In this paper, we have presented an energy conserving lattice Boltzmann model which is suitable for compressible hydrodynamics, aeroacoustics, and thermoacoustic problems. It recovers the pressure dynamics and the isentropic sound speed in addition to the effects of viscous heating, and heat conduction with a high degree of accuracy. The theoretical requirements and the methodology to construct this model have been discussed, and the test cases confirm its stability for a wide range of parameters. With improved accuracy in the velocity space and better representation of the curved surfaces, this model raises the prospect of direct simulations of turbulent flows involving objects. This has been shown via simulations of Kida-Pelz flow, channel flow and flow past a sphere. The specific heat ratio and Prandtl number of this model are fixed. This restriction on the Prandtl number can be addressed by a number of collision kernels [102–105]. The interactions between turbulence and acoustics along with methods to fix the specific heat ratio to that of polyatomic gases is subject of further investigation [106].

ACKNOWLEDGMENTS

The authors would like to thank S. Bhattacharya for his help in generating Fig. 2. We also acknowledge C. Thantana-pally for sharing his pseudospectral routines.

APPENDIX: EVALUATING DERIVATIVES ON A LATTICE

In this Appendix, we briefly review the way to evaluate the discrete gradients and Laplacian in an isotropic manner. The

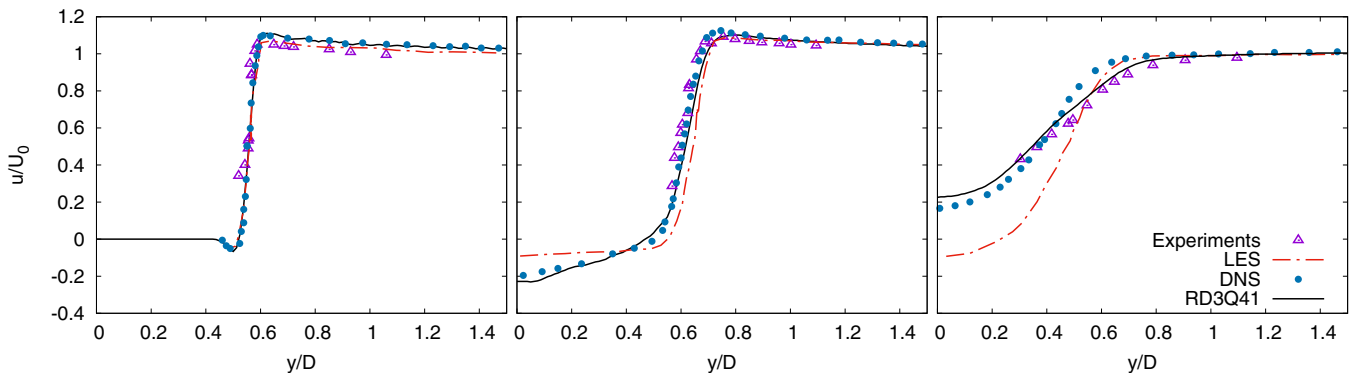


FIG. 26. Averaged profile of the normalized velocity at three different locations ($x/D = 0.2, 1.6, 3.0$) in the wake of the sphere from this study (solid line) compared with DNS [98], LES [99], and experimental [100] studies.

discrete derivative $\tilde{\partial}$ is defined as

$$\tilde{\partial}_\alpha \psi = \frac{1}{\hat{\theta}_0 \Delta t} \sum_i \hat{w}_i c_{i\alpha} \psi(\mathbf{x} + \mathbf{c}_i \Delta t). \quad (\text{A1})$$

Here, \hat{w}_i are the weights of the lattice with discrete velocities $c_{i\alpha}$ and ψ is the function whose derivative needs to be calculated. The above definition can be understood as follows: we consider the Taylor expansion of $Q_\alpha = \sum_i \hat{w}_i c_{i\alpha} \psi(\mathbf{x} + \mathbf{c}_i \Delta t) / (\hat{\theta}_0 \Delta t)$ [107,108],

$$\begin{aligned} Q_\alpha &\equiv \frac{1}{\hat{\theta}_0 \Delta t} \sum_i \hat{w}_i c_{i\alpha} \psi(\mathbf{x} + \mathbf{c}_i \Delta t) = \frac{1}{\hat{\theta}_0 \Delta t} \left[\psi(\mathbf{x}) \sum_i \hat{w}_i c_{i\alpha} \right. \\ &+ \Delta t \frac{\partial \psi}{\partial x_\beta} \sum_i \hat{w}_i c_{i\alpha} c_{i\beta} + \frac{\Delta t^2}{2} \frac{\partial^2 \psi}{\partial x_\beta \partial x_\gamma} \sum_i \hat{w}_i c_{i\alpha} c_{i\beta} c_{i\gamma} \\ &\left. + \frac{\Delta t^3}{6} \frac{\partial^3 \psi}{\partial x_\beta \partial x_\gamma \partial x_\kappa} \sum_i \hat{w}_i c_{i\alpha} c_{i\beta} c_{i\gamma} c_{i\kappa} + O(\Delta t^4) \right]. \end{aligned} \quad (\text{A2})$$

The odd-order moments of weight are zero due to symmetry of the underlying lattice and further simplification of Q_α leads to

$$\begin{aligned} Q_\alpha &\equiv \frac{1}{\hat{\theta}_0 \Delta t} \sum_i \hat{w}_i c_{i\alpha} \psi(\mathbf{x} + \mathbf{c}_i \Delta t) = \frac{\partial \psi}{\partial x_\alpha} \\ &+ \frac{\Delta t^2 \hat{\theta}_0}{2} \frac{\partial}{\partial x_\alpha} \partial^2 \psi + \frac{3 \Delta t^4 \hat{\theta}_0^2}{8} \frac{\partial}{\partial x_\alpha} \partial^4 \psi + O(\Delta t^6), \end{aligned} \quad (\text{A3})$$

assuming the lattice is sufficiently isotropic. The emergence of the derivatives of ψ is seen on the right-hand side of the above equation.

The second-order gradient is hence

$$\tilde{\partial}_\alpha^{(2)} \psi = \frac{1}{\hat{\theta}_0 \Delta t} \sum_i \hat{w}_i c_{i\alpha} \psi(\mathbf{x} + \mathbf{c}_i \Delta t). \quad (\text{A4})$$

The fourth-order gradient is written as

$$\tilde{\partial}_\alpha^{(4)} \psi = \frac{1}{\hat{\theta}_0 \Delta t} \sum_i \hat{w}_i c_{i\alpha} \psi(\mathbf{x} + \mathbf{c}_i \Delta t) - \frac{\hat{\theta}_0}{2} (\Delta t)^2 \nabla_\alpha (\nabla^2 \psi). \quad (\text{A5})$$

The Laplacian can also be evaluated as

$$\tilde{\partial}^2 \psi = \frac{2}{\Delta t^2 \hat{\theta}_0} \left[\sum_i \hat{w}_i \psi(\mathbf{x} + \mathbf{c}_i \Delta t) - \psi(\mathbf{x}) \right]. \quad (\text{A6})$$

Here, it remains to justify the choice of stencil for calculating derivatives. From Eq. (A3) it is evident that the discretization errors are proportional to $\hat{\theta}_0 = \sum \hat{w}_i c_{i\alpha}^2$ of the chosen stencil. For the crystallographic grid, the 15 velocity stencil comprising of the discrete velocities

$$c_i = \{(\pm 1, 0, 0), (0, \pm 1, 0), (0, 0, \pm 1), (\pm 0.5, \pm 0.5, \pm 0.5)\} \quad (\text{A7})$$

is found to have the least $\hat{\theta}_0 = \frac{1}{6}$ with $\hat{w}_0 = \frac{14}{36}$, $\hat{w}_{\text{SC}} = \frac{1}{36}$, and $\hat{w}_{\text{BCC}} = \frac{2}{36}$, therefore, is the ideal choice for computing derivatives.

-
- [1] S. Succi, *The Lattice Boltzmann Equation: For Fluid Dynamics and Beyond* (Oxford University Press, Oxford, 2001).
- [2] S. Chen and G. D. Doolen, *Annu. Rev. Fluid Mech.* **30**, 329 (1998).
- [3] C. K. Aidun and J. R. Clausen, *Annu. Rev. Fluid Mech.* **42**, 439 (2010).
- [4] S. Ansumali and I. V. Karlin, *Phys. Rev. Lett.* **95**, 260605 (2005).
- [5] P. J. Dellar, *Phys. Rev. E* **64**, 031203 (2001).
- [6] M. Namburi, S. Krithivasan, and S. Ansumali, *Sci. Rep.* **6**, 27172 (2016).
- [7] A. J. Ladd, *J. Fluid Mech.* **271**, 285 (1994).
- [8] A. Ladd and R. Verberg, *J. Stat. Phys.* **104**, 1191 (2001).
- [9] A. J. C. Ladd, *Phys. Rev. Lett.* **70**, 1339 (1993).
- [10] J. Buick, C. Greated, and D. Campbell, *Europhys. Lett.* **43**, 235 (1998).
- [11] B. Crouse, D. Freed, G. Balasubramanian, S. Senthoooran, P. T. Lew, and L. Mongeau, in *12th AIAA/CEAS Aeroacoustics Conference (27th AIAA Aeroacoustics Conference)* (AIAA, Reston, VA, 2006), p. 2571.
- [12] S. Marié, D. Ricot, and P. Sagaut, *J. Comput. Phys.* **228**, 1056 (2009).
- [13] Y. Li and X. Shan, *Philos. Trans. R. Soc. London A* **369**, 2371 (2011).
- [14] E. M. Vigen, *Phys. Rev. E* **87**, 023306 (2013).
- [15] E. M. Vigen, *Phys. Rev. E* **90**, 013310 (2014).
- [16] L. D. Landau and E. Lifshitz, *Course of Theoretical Physics, Vol. 6, Fluid Mechanics* (Pergamon, Oxford, 1959).
- [17] P. M. Chaikin and T. C. Lubensky, *Principles of Condensed Matter Physics* (Cambridge University Press, Cambridge, 2000), Vol. 1.
- [18] H. B. Callen, *Thermodynamics and an Introduction to Thermostatistics* (Wiley, New York, 1985).
- [19] L. G. Leal, *Advanced Transport Phenomena: Fluid Mechanics and Convective Transport Processes* (Cambridge University Press, Cambridge, 2007), Vol. 7.
- [20] S. Singh, S. Krithivasan, I. V. Karlin, S. Succi, and S. Ansumali, *Commun. Comput. Phys.* **13**, 603 (2013).
- [21] N. Prasianakis and K. Boulouchos, *Int. J. Mod. Phys. C* **18**, 602 (2007).
- [22] N. I. Prasianakis and I. V. Karlin, *Phys. Rev. E* **78**, 016704 (2008).
- [23] S. Ansumali, I. V. Karlin, and H. C. Öttinger, *Europhys. Lett.* **63**, 798 (2003).
- [24] J. Kang, N. I. Prasianakis, and J. Mantzaras, *Phys. Rev. E* **87**, 053304 (2013).
- [25] N. I. Prasianakis, I. V. Karlin, J. Mantzaras, and K. B. Boulouchos, *Phys. Rev. E* **79**, 066702 (2009).
- [26] N. Frapolli, S. S. Chikatamarla, and I. V. Karlin, *Phys. Rev. E* **90**, 043306 (2014).
- [27] M. Atif, M. Namburi, and S. Ansumali, *Phys. Rev. E* **98**, 053311 (2018).

- [28] W. P. Yudistiawan, S. K. Kwak, D. V. Patil, and S. Ansumali, *Phys. Rev. E* **82**, 046701 (2010).
- [29] P. L. Bhatnagar, E. P. Gross, and M. Krook, *Phys. Rev.* **94**, 511 (1954).
- [30] A. J. Wagner, *Europhys. Lett.* **44**, 144 (1998).
- [31] H. Chen, S. Chen, and W. H. Matthaeus, *Phys. Rev. A* **45**, R5339(R) (1992).
- [32] Y. Qian, D. d'Humières, and P. Lallemand, *Europhys. Lett.* **17**, 479 (1992).
- [33] R. Benzi, S. Succi, and M. Vergassola, *Phys. Rep.* **222**, 145 (1992).
- [34] X. Shan and X. He, *Phys. Rev. Lett.* **80**, 65 (1998).
- [35] S. S. Chikatamarla and I. V. Karlin, *Phys. Rev. E* **79**, 046701 (2009).
- [36] W. P. Yudistiawan, S. Ansumali, and I. V. Karlin, *Phys. Rev. E* **78**, 016705 (2008).
- [37] S. S. Chikatamarla and I. V. Karlin, *Phys. Rev. Lett.* **97**, 190601 (2006).
- [38] Y.-H. Qian and Y. Zhou, *Europhys. Lett.* **42**, 359 (1998).
- [39] X. Shan, X.-F. Yuan, and H. Chen, *J. Fluid Mech.* **550**, 413 (2006).
- [40] S. Chikatamarla, C. Frouzakis, I. Karlin, A. Tomboulides, and K. Boulouchos, *J. Fluid Mech.* **656**, 298 (2010).
- [41] L. E. Reichl, *A Modern Course in Statistical Physics* (Wiley, Weinheim, 1999).
- [42] R. L. Liboff, *Kinetic Theory: Classical, Quantum, and Relativistic Descriptions* (Springer, New York, 2003).
- [43] A. Mazloomi M, S. S. Chikatamarla, and I. V. Karlin, *Phys. Rev. Lett.* **114**, 174502 (2015).
- [44] J. S. N. Murthy, P. K. Kolluru, V. Kumaran, and S. Ansumali, *Commun. Comput. Phys.* **23**, 1223 (2018).
- [45] U. R. Alim, A. Entezari, and T. Möller, *IEEE Trans. Vis. Comput. Graph.* **15**, 630 (2009).
- [46] S. Ansumali, I. V. Karlin, S. Arcidiacono, A. Abbas, and N. I. Prasianakis, *Phys. Rev. Lett.* **98**, 124502 (2007).
- [47] I. V. Karlin, A. N. Gorban, S. Succi, and V. Boffi, *Phys. Rev. Lett.* **81**, 6 (1998).
- [48] B. M. Boghosian, P. J. Love, P. V. Coveney, I. V. Karlin, S. Succi, and J. Yepez, *Phys. Rev. E* **68**, 025103(R) (2003).
- [49] H. Chen and C. Teixeira, *Comput. Phys. Commun.* **129**, 21 (2000).
- [50] I. V. Karlin, A. Ferrante, and H. C. Öttinger, *Europhys. Lett.* **47**, 182 (1999).
- [51] S. Succi, I. V. Karlin, and H. Chen, *Rev. Mod. Phys.* **74**, 1203 (2002).
- [52] S. S. Chikatamarla, S. Ansumali, and I. V. Karlin, *Phys. Rev. Lett.* **97**, 010201 (2006).
- [53] C. K. Tam and J. C. Webb, *J. Comput. Phys.* **107**, 262 (1993).
- [54] F. Gendre, D. Ricot, G. Fritz, and P. Sagaut, *Phys. Rev. E* **96**, 023311 (2017).
- [55] M. Abramowitz and I. A. Stegun, *Handbook of Mathematical Functions: With Formulas, Graphs, and Mathematical Tables* (Dover, New York, 1965), Vol. 55.
- [56] C. Bogey and C. Bailly, *Acta Acoust. United Ac.* **88**, 463 (2002).
- [57] J. Hardin, J. Ristorcelli, and C. Tam, *ICASE/LaRC Workshop on Benchmark Problems in Computational Aeroacoustics* (NASA Langley Research Center, Hampton, VA, 1994).
- [58] C. K. Tam and J. Hardin, *Second Computational Aeroacoustics (CAA) Workshop on Benchmark Problems* (NASA Langley Research Center, Hampton, VA, 1997).
- [59] C. Tam and F. Hu, in *10th AIAA/CEAS Aeroacoustics Conference* (AIAA, Reston, VA, 2004), p. 2812.
- [60] R. B. Bird, W. E. Stewart, E. N. Lightfoot, and D. J. Klingenberg, *Introductory Transport Phenomena* (Wiley, New York, 2015), Vol. 1.
- [61] S. Ansumali and I. V. Karlin, *Phys. Rev. E* **66**, 026311 (2002).
- [62] B. Larkin, in *Thermophysics of Spacecraft and Planetary Bodies* (Elsevier, Amsterdam, 1967), pp. 819–832.
- [63] M. Parang and A. Salah-Eddine, *AIAA J.* **22**, 1020 (1984).
- [64] Y. Huang and H. H. Bau, *Int. J. Heat Mass Transfer* **40**, 407 (1997).
- [65] L. W. Spradley and S. W. Churchill, *J. Fluid Mech.* **70**, 705 (1975).
- [66] Y. Huang and H. H. Bau, *Int. J. Heat Mass Transfer* **38**, 1329 (1995).
- [67] A. K. Gunstensen, D. H. Rothman, S. Zaleski, and G. Zanetti, *Phys. Rev. A* **43**, 4320 (1991).
- [68] X. Shan and H. Chen, *Phys. Rev. E* **47**, 1815 (1993).
- [69] M. R. Swift, W. R. Osborn, and J. M. Yeomans, *Phys. Rev. Lett.* **75**, 830 (1995).
- [70] X. He, X. Shan, and G. D. Doolen, *Phys. Rev. E* **57**, R13(R) (1998).
- [71] S. Ansumali, *Commun. Comput. Phys.* **9**, 1106 (2011).
- [72] X. He and G. D. Doolen, *J. Stat. Phys.* **107**, 309 (2002).
- [73] T. Lee and P. F. Fischer, *Phys. Rev. E* **74**, 046709 (2006).
- [74] X. Shan, *Phys. Rev. E* **73**, 047701 (2006).
- [75] A. J. Wagner, *Phys. Rev. E* **74**, 056703 (2006).
- [76] J. D. van der Waals, *J. Stat. Phys.* **20**, 200 (1979).
- [77] J. Rowlinson and B. Widom, *Molecular Theory of Capillarity* (Clarendon, Oxford, 1982).
- [78] T. Lee and C.-L. Lin, *J. Comput. Phys.* **206**, 16 (2005).
- [79] S. Suryanarayanan, S. Singh, and S. Ansumali, *Commun. Comput. Phys.* **13**, 629 (2013).
- [80] D. J. Korteweg, *Arch. Neerl. Sci. Exactes Nat. Ser. II* **6**, 1 (1901).
- [81] R. Evans, *Adv. Phys.* **28**, 143 (1979).
- [82] A. J. Wagner and C. M. Pooley, *Phys. Rev. E* **76**, 045702(R) (2007).
- [83] N. F. Carnahan and K. E. Starling, *J. Chem. Phys.* **51**, 635 (1969).
- [84] T. Inamuro, S. Tajima, and F. Ogino, *Int. J. Heat Mass Transfer* **47**, 4649 (2004).
- [85] M. Atif, P. K. Kolluru, C. Thantapanally, and S. Ansumali, *Phys. Rev. Lett.* **119**, 240602 (2017).
- [86] S. Kida, *J. Phys. Soc. Jpn.* **54**, 2132 (1985).
- [87] U. Frisch, *Turbulence: The Legacy of AN Kolmogorov* (Cambridge University Press, Cambridge, 1995).
- [88] C. Thantapanally, D. V. Patil, S. Succi, and S. Ansumali, *J. Fluid Mech.* **728**, R4 (2013).
- [89] C. Canuto, M. Y. Hussaini, A. Quarteroni, A. Thomas Jr. et al., *Spectral Methods in Fluid Dynamics* (Springer, New York, 2012).
- [90] M. Frigo and S. G. Johnson, *Proc. IEEE* **93**, 216 (2005).

- [91] C. Thantapanally, Saturation of vorticity growth in fully-developed fluid turbulence, Master's thesis, Jawaharlal Nehru Centre for Advanced Scientific Research, 2013.
- [92] R. Bridson, J. Houriham, and M. Nordenstam, *ACM Trans. Graph* **26**, 46 (2007).
- [93] S. B. Pope, *Turbulent Flows* (Cambridge University Press, Cambridge, 2001).
- [94] R. D. Moser, J. Kim, and N. N. Mansour, *Phys. Fluids* **11**, 943 (1999).
- [95] J. Kim, P. Moin, and R. Moser, *J. Fluid Mech.* **177**, 133 (1987).
- [96] S. Chikatamarla, S. Ansumali, and I. Karlin, *Europhys. Lett.* **74**, 215 (2006).
- [97] S. Krithivasan, S. Wahal, and S. Ansumali, *Phys. Rev. E* **89**, 033313 (2014).
- [98] I. Rodríguez, O. Lehmkuhl, R. Borrell, and A. Oliva, *Comput. Fluids* **80**, 233 (2013).
- [99] G. Yun, D. Kim, and H. Choi, *Phys. Fluids* **18**, 015102 (2006).
- [100] H. Kim and P. Durbin, *Phys. Fluids* **31**, 3260 (1988).
- [101] B. Dorschner, N. Frapolli, S. S. Chikatamarla, and I. V. Karlin, *Phys. Rev. E* **94**, 053311 (2016).
- [102] L. H. Holway Jr, *Phys. Fluids* **9**, 1658 (1966).
- [103] E. M. Shakhov, *Fluid Dyn.* **3**, 95 (1968).
- [104] C. D. Levermore, *J. Stat. Phys.* **83**, 1021 (1996).
- [105] S. Ansumali, S. Arcidiacono, S. Chikatamarla, N. Prasianakis, A. Gorban, and I. Karlin, *Eur. Phys. J. B* **56**, 135 (2007).
- [106] X. Nie, X. Shan, and H. Chen, *Phys. Rev. E* **77**, 035701(R) (2008).
- [107] S. P. Thampi, S. Ansumali, R. Adhikari, and S. Succi, *J. Comput. Phys.* **234**, 1 (2013).
- [108] R. Ramadugu, S. P. Thampi, R. Adhikari, S. Succi, and S. Ansumali, *Europhys. Lett.* **101**, 50006 (2013).